

## Article

# Evolution in Wear and High-Temperature Oxidation Resistance of Laser-Clad Al<sub>x</sub>MoNbTa Refractory High-Entropy Alloys Coatings with Al Addition Content

Sichun Hong, Jun Li <sup>\*</sup>, Peng Zhao, Yinsi Xu and Wanggen Li

School of Materials Engineering, Shanghai University of Engineering Science, Shanghai 201620, China; celina19821391807@163.com (S.H.); cecilia19821391807@yeah.net (P.Z.); 18238237071@163.com (Y.X.); lwg2020Y@163.com (W.L.)

\* Correspondence: jacob\_lijun@sues.edu.cn; Tel.: +86-21-6779-1198; Fax: +86-21-6779-1377

**Abstract:** Al<sub>x</sub>MoNbTa (x = 0.5, 1.0 and 1.5) refractory high-entropy alloy (RHEAs) coatings were produced on Ti6Al4V by laser cladding. Ti<sub>2</sub>AlNb as the second phase and the solid solutions with the body center cubic structure (BCC) as the matrix were synthesized in the coatings. The average microhardness of the coatings was increased with the increase in x, along with which the fracture toughness was decreased. Wear resistance of the coatings was investigated by the dry-sliding reciprocating wear tests at room temperature in air (Si<sub>3</sub>N<sub>4</sub> as the counterparts, the 10 N load for 30 min, and the 3 mm/s sliding speed). The wear rate of the coatings was decreased with x enhanced from 0.5 (6.34 × 10<sup>-5</sup> mm<sup>3</sup>/N·m) to 1.0 (5.90 × 10<sup>-5</sup> mm<sup>3</sup>/N·m), then slightly increased with x enhanced to 1.5 (6.18 × 10<sup>-5</sup> mm<sup>3</sup>/N·m). Oxidation resistance was evaluated by the high-temperature oxidation tests at 1000 °C in air for 120 h. The whole mass gain of the coatings showed a slight downward tendency (61.8 mg/cm<sup>2</sup> for x = 0.5, 57.8 mg/cm<sup>2</sup> for x = 1.0 and 56.3 mg/cm<sup>2</sup> for x = 1.5). The change in wear and oxidation mechanism with x was revealed in detail.

**Keywords:** high-entropy alloys coating; laser cladding; mechanical properties; wear resistance; oxidation resistance



**Citation:** Hong, S.; Li, J.; Zhao, P.; Xu, Y.; Li, W. Evolution in Wear and High-Temperature Oxidation Resistance of Laser-Clad Al<sub>x</sub>MoNbTa Refractory High-Entropy Alloys Coatings with Al Addition Content. *Coatings* **2022**, *12*, 121. <https://doi.org/10.3390/coatings12020121>

Academic Editor: Hideyuki Murakami

Received: 29 November 2021

Accepted: 19 January 2022

Published: 21 January 2022

**Publisher's Note:** MDPI stays neutral with regard to jurisdictional claims in published maps and institutional affiliations.



**Copyright:** © 2022 by the authors. Licensee MDPI, Basel, Switzerland. This article is an open access article distributed under the terms and conditions of the Creative Commons Attribution (CC BY) license (<https://creativecommons.org/licenses/by/4.0/>).

## 1. Introduction

With the rapid development of engineering technology, the Ti6Al4V alloy is widely used in many industrial applications, including marine, aeronautical, chemical industries, power generation, biomedical devices, sport and entertainment facilities, and transportation due to its high strength-to-weight ratio, excellent corrosion resistance and good biocompatibility, etc. [1–3]. However, poor wear resistance and high-temperature oxidation resistance restrict its engineering applications in wear and oxidation circumstances [2,4]. Many surface modification methods have been applied to solve the above-mentioned shortcomings involved in Ti6Al4V, such as plasma spray [5], ion implantation [6], sol-gel [7], micro-arc oxidation [8], magnetron sputtering [9] and selective laser melting [10]. Among them, laser cladding technology has attracted attention since the fused microstructure is very dense and can be flexibly controlled by selecting the different laser-clad materials. Moreover, the thickness of coatings can be adjusted from micron to millimeter and they have a strong metallurgical bonding to the substrates [11–13]. Different ceramic particle-reinforced metal matrix coatings have been explored (TiC–NiCrBSi composite coatings [14], TiC/Ti<sub>5</sub>Si<sub>3</sub> reinforced titanium matrix coatings [15], TiC/TiB<sub>2</sub>/TiB reinforced nickel-based coatings [16], TiC/TiB<sub>2</sub>/Ti<sub>2</sub>Ni reinforced titanium matrix coatings [17], Ti<sub>2</sub>Ni/Ti<sub>5</sub>Si<sub>3</sub>/TiSi reinforced titanium matrix coatings [18]). Nevertheless, some new challenges, like high cracking sensitivity and poor processing performance, are presented in these coatings. Therefore, it is very necessary to seek a strategy to synthesize a new coating, which possesses high microhardness and plasticity. Yeh et al. [19] put forward a concept, namely multi-component

high-entropy alloys (HEAs). HEAs mainly consist of solid solutions, which, accompanied by a small amount of intermetallic compound, may be precipitated. Therefore, the HEAs can maintain a high microhardness and strength without seriously reducing plasticity [20,21]. Moreover, the HEAs possess the other promising properties, such as superior thermal stability [22], excellent oxidation resistance [23,24], high wear and corrosion resistance [25–27], and so on. It can be concluded that the HEA coatings prepared by laser cladding are expected to be endowed with excellent wear and high-temperature oxidation resistance. Some researchers have proven this. Li et al. [28] deposited the  $\text{Al}_x\text{CrFeCoNiCu}$  HEA coatings on aluminum by laser cladding, the wear rates of which were lower than that of the substrate ( $3.50 \times 10^{-4} \text{ mm}^3/\text{N}\cdot\text{m}$ ) and reduced as increasing  $x$  ( $2.26 \times 10^{-4} \text{ mm}^3/\text{N}\cdot\text{m}$  for  $x = 0$ ,  $1.95 \times 10^{-5} \text{ mm}^3/\text{N}\cdot\text{m}$  for  $x = 0.8$  and  $6.6 \times 10^{-7} \text{ mm}^3/\text{N}\cdot\text{m}$  for  $x = 1.5$ ). Chang et al. [29] prepared the  $\text{FeCr}_x\text{CoNiB}$  ( $x$  values in molar ratio,  $x = 0.5\text{--}3.0$ ) HEA coatings on AISI 1045 steel and carried out the high-temperature oxidation experiments at  $900^\circ\text{C}$ . The oxidation mass gain of the coatings ( $3 \text{ mg}/\text{cm}^2$  for  $x = 3.0$ ) was lower than that of the substrate ( $15 \text{ mg}/\text{cm}^2$ ), and the oxidation kinetics curve of coatings fitted well with the parabolic law, whereas that of the substrate was a straight line. Zhang et al. [30] synthesized the  $\text{AlCoCrFeNiSi}$  HEA coatings on AISI 304 stainless steel by laser cladding. The average microhardness of the coating ( $630.36 \text{ HV}_{0.3}$ ) was three times higher than that of the substrate ( $210 \text{ HV}_{0.3}$ ) due to the solid solution strengthening effect. The wear rate of the coating ( $4.2 \times 10^{-4} \text{ mm}^3/\text{N}\cdot\text{m}$ ) was about 0.09 times that of the substrate ( $4.5 \times 10^{-3} \text{ mm}^3/\text{N}\cdot\text{m}$ ).

In 2010, Senkov et al. [31] introduced refractory high-entropy alloys (RHEAs), which were composed of high melting point metals including Hf, Ta, Nb, Zr, Ti, V, W, Mo and Cr [32–34]. Some investigations had shown that the RHEAs demonstrated the more outstanding high-temperature oxidation resistance when compared with the traditional superalloys [35,36]. The introduction of Al into the RHEAs had been proved to improve the high-temperature oxidation resistance of the RHEAs [37,38]. Cao et al. [37] fabricated the  $\text{TiNbTa}_{0.5}\text{ZrAl}$  and  $\text{TiNbTa}_{0.5}\text{Zr}$  RHEAs by the vacuum arc technology and carried out the isothermal oxidation tests of RHEAs in air. The mass gain of  $\text{TiNbTa}_{0.5}\text{ZrAl}$  was about  $40 \text{ mg}/\text{cm}^2$  when subject to the high-temperature oxidation at  $1000^\circ\text{C}$  for 40 h, which was 25% that of  $\text{TiNbTa}_{0.5}\text{Zr}$  ( $160 \text{ mg}/\text{cm}^2$ ). The change should be attributed to the formation of dense, intact, well-adhered and protective  $\text{Al}_2\text{O}_3$  layers on  $\text{TiNbTa}_{0.5}\text{ZrAl}$ . Jayaraj et al. [38] prepared the  $\text{AlNbTiZr}$  and  $\text{HfNbTiZr}$  by using the same technology and carried out the isothermal thermo-gravimetry tests of the samples in air. The mass gain of  $\text{AlNbTiZr}$  was about  $1 \text{ mg}/\text{cm}^2$  when suffering from the high-temperature oxidation at  $600^\circ\text{C}$  for 3 h, which was much lower than that of  $\text{HfNbTiZr}$  ( $6 \text{ mg}/\text{cm}^2$ ). The results indicated the replacing Hf in  $\text{HfNbTiZr}$  with Al significantly improved the high-temperature oxidation resistance of the RHEAs. Chen et al. [39] successfully fabricated an  $\text{TiVMoNb}$  RHEA coating with the addition of Al on Ti6Al4V laser cladding and evaluated its high-temperature oxidation resistance at  $800^\circ\text{C}$  for 120 h in air. The oxidation mass gain was only 10.6% that of the substrate (Ti6Al4V). Besides the improvement in high-temperature oxidation resistance, the introduction of Al is also beneficial to the reduction in density of RHEAs because of its lower density ( $\rho_{\text{Al}} = 2.70 \text{ g}/\text{cm}^3$ ) than the majority of commonly used refractory metals ( $\rho_{\text{Hf}} = 13.31 \text{ g}/\text{cm}^3$ ,  $\rho_{\text{Mo}} = 10.22 \text{ g}/\text{cm}^3$ ,  $\rho_{\text{Nb}} = 8.57 \text{ g}/\text{cm}^3$ ,  $\rho_{\text{Ta}} = 16.68 \text{ g}/\text{cm}^3$ ) [40,41]. Moreover, the mismatch in atomic radius between Al and commonly used refractory metals also contributes to aggravating the lattice distortion, further enhancing wear resistance due to the improvement in microhardness/strength. Bhardwaj et al. [42] fabricated several  $\text{Al}_x\text{TiZrNbHf}$  RHEAs with different  $x$  value ( $x = 0, 0.25, 0.50, 0.75, 1.0$ ) by arc melting technique and studied the effect of Al addition on its microstructure, mechanical and wear properties. The microhardness greatly increased from 229 HV to 420 HV with the enhancement of Al addition. The wear mechanism of  $\text{TiZrNbHf}$  and  $\text{Al}_{0.25}\text{TiZrNbHf}$  RHEAs with a low microhardness value was found to be serious adhesion wear because of more plastic and surface deformation on the wear tracks whereas  $\text{Al}_{1.0}\text{TiZrNbHf}$  RHEAs was oxidative wear. The difference in wear mechanism resulted in the  $\text{Al}_x\text{TiZrNbHf}$  RHEA with a higher content demonstrating more outstanding wear resistance ( $0.045 \text{ mm}^3$

and  $0.065 \text{ mm}^3$  in wear volume of the AlTiZrNbHf and TiZrNbHf RHEAs). The other RHEAs with the addition of Al ( $\text{Al}_{0.4}\text{Hf}_{0.6}\text{NbTaTiZr}$  [43],  $\text{AlNbTaTiV}$  [44] and  $\text{AlNbTiV}$  [45], etc.) also confirmed the positive role produced by the introduction of Al. However, the comprehensive investigations into the effects of the content of Al on wear resistance and high-temperature oxidation resistance of the RHEAs fabricated by laser cladding were rarely reported.

In our research,  $\text{Al}_x\text{MoNbTa}$  ( $x = 0.5, 1.0$  and  $1.5$  in molar ratio) was chosen as the cladding material to prepare  $\text{Al}_x\text{MoNbTa}$  RHEAs coatings on Ti6Al4V by laser cladding. The effects of Al addition on phase constituent, microstructure, mechanical properties (microhardness, fracture toughness, wear resistance), and high-temperature oxidation resistance of the Al-doped RHEAs coatings are systematically investigated. With the increase in Al addition content, the evolution in mechanism of both wear and high-temperature oxidation was analyzed in detail. Based on them, the suitable addition content of Al was ascertained.

## 2. Materials and Methods

### 2.1. Fabrication of Laser-Clad Coatings

Ti6Al4V was chosen as a substrate and was processed into a cylinder with a 10.0 mm height and a 50.0 mm diameter. Commercial Al, Mo, Nb and Ta powders ( $10\text{--}20 \mu\text{m}$ , Sinopharm Chemical Reagent Co., Ltd., Shanghai, China) with a high purity of  $\geq 99 \text{ wt.}\%$  were chosen as the precursors for laser cladding, which were weighted and mixed in the three proportions ( $\text{Al}_x\text{MoNbTa}$ ,  $x = 0.5, x = 1.0$  and  $x = 1.5$ ). Powders were placed in a polytetrafluoroethylene grinding tank, and then milled at  $300 \text{ r/min}$  for 8 h on a QM-3SP2 planetary ball milling. The preset layer was first prepared (Figure 1). A thin layer of adhesive (4% polyvinyl alcohol) was brushed on the surface of the substrate and the coated substrate was placed into a hollow cylinder of 11.0 mm in height and 52.0 mm in inner diameter. The mixed powder was fed into the void above the substrate to form a loose powder layer with a height of 1.0 mm. Then a tablet press was used to compress the powder layer at  $30 \text{ MPa}$  for 3 min to form a compact preset layer with a thickness of approximately 0.8 mm.

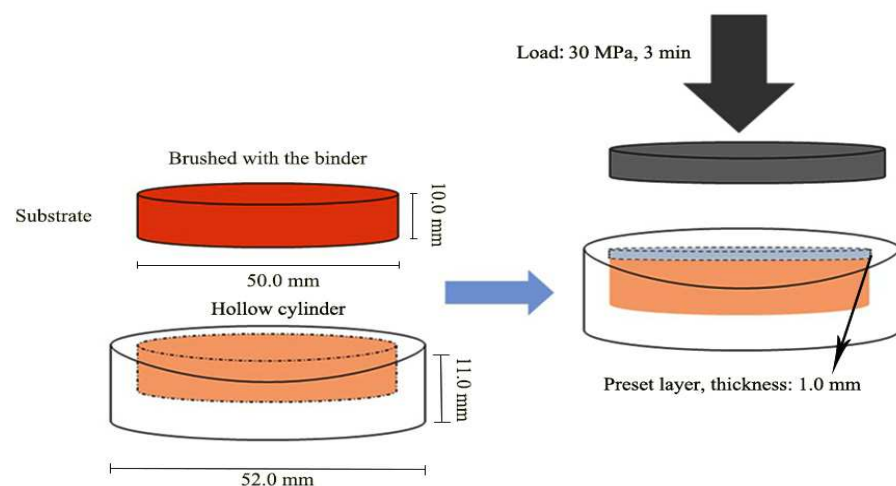


**Figure 1.** The schematic drawing of the preparation process of the preset layer.

Laser cladding was performed using an YLS-5000 fiber laser system (IPG Photonics Corporation, Oxford, MS, USA). The samples were placed in a chamber made of stainless steel filled with argon of a standard pressure at room temperature, which prevented oxygen from invading the molten pool during laser cladding. The laser beam moved along the X direction with 3 kW in output laser power, 5 mm/s in laser scanning speed and 6 mm in spot diameter. The scanning direction will produce the significant effect on the morphology and microstructure of the coatings, which may cause the anisotropy. The

energy in the laser beam follows the Gaussian distribution, namely, the energy is mainly focused in the middle of the laser beam, and presents the gradual downward tendency with increasing the distance from the middle. Therefore, the middle of the molten track will suffer from the sufficient melting and form the wavy pattern along the scanning direction [46]. The side of the molten track subject to the poor radiation may be surrounded by unmelted powders, which may adhere together due to a portion of heat flowing to these powders. The difference in energy distribution also causes the formation of a crescent profile regarding the cross sections of coatings, in which the thickness and the molten track is largest in the middle, and is gradually decreased with the increase in distance from the middle. Besides these, the microstructure is also associated with the scanning direction. Regarding the direction perpendicular to the scanning direction for a given cross section, the microstructure demonstrates the anisotropy due to the difference in temperature gradient ( $G$ ) and growth rate ( $V$ ). The value of  $G/V$  is responsible for the microstructure based on the columnar to equiaxed transition model [47]. The solidification begins from the bottom of the molten pool with a greatest  $G/V$  by the epitaxial growth. With the solid/liquid interface gradually proceeding, the microstructure is transformed to cellular crystals, columnar dendrites, finally equiaxed dendrites due to the gradual reduction in  $G/V$ .

## 2.2. Microstructural Characterization

The phase constituents of the coatings were identified by using a Panalytical X'Pert Pro X-ray diffractometer (XRD, Malvern Panalytical Co., Ltd., Shanghai, China) with  $\text{Cu K}\alpha$  radiation ( $\lambda = 0.1540560$  nm). Morphologies and chemical compositions of the coatings were analyzed by using a Hitachi S-3400 scanning electron microscope (SEM, Hitachi, Tokyo, Japan) and a Genesis EDAX energy spectrometer (EDS, EDAX Inc., Philadelphia, PA, USA). Before the tests, the cross-sections of samples were ground with 150, 600 and 1200 grit SiC abrasive papers in turn and then polished with the  $1.0 \mu\text{m}$  diamond paste. Finally, these samples were etched for 30 s in a mixed solution containing 4 mL  $\text{H}_2\text{O}$ , 6 mL  $\text{HNO}_3$  and 8 drops of HF.

## 2.3. Mechanical Properties Testing

The microhardness of the coatings was examined using an HXD-1000TMSC/LCD Vickers microhardness tester (Shanghai Taiming Optical Instrument Co., Ltd., Shanghai, China) with an applied load of 200 gf load and a dwelling time of 15 s. The microhardness value was measured along the depth direction, and 0.1 mm interval was maintained between the two adjacent testing zones. For the zones with the same distance from the surfaces of the coatings, three microhardness values were tested and the average value was calculated. The microhardness of the specific micro-zones was also identified by the Vickers indentations with a small applied load of 10 gf for 15 s. The microhardness can be applied to characterize the resistance to plastic deformation of the coating. The high microhardness means that it is difficult to impress an object into the coating under the external force, namely the coatings possess the strong resistance to micro cutting when the two do the relative motion.

The fracture toughness ( $K_{IC}$ ) value was tested by the Vickers indentation method on an HV-120 Vickers hardness tester (Shanghai Material testing Machine Factory, Shanghai, China) with 5 kgf load for 15 s. Three indentations were obtained in the middle of each coatings, and their morphologies were observed to measure half the indentation's diagonal length ( $a$ ) and half of the total length of the diagonal and the crack by a VHX-600K optical microscope (OM) (Shanghai Dilun Optical Instrument Co., Ltd., Shanghai, China). Then the fracture toughness was calculated by the following formula [48].

$$K_{IC} = 0.079P \left\{ \frac{P}{(a)^{\frac{3}{2}}} \right\} \log \left( 4.5 \frac{a}{c} \right) \quad (1)$$

In which, the  $K_{IC}$  value stands for fracture toughness,  $p$  denotes the load;  $a$  represents half of the indentation's diagonal length; and  $c$  signifies half of the total length of the diagonal and the crack.

Dry sliding friction tests were conducted by a CFT-1 multifunctional wear tester (Lanzhou Zhongke Kaihua Technology Development Co., Ltd., Lanzhou, China) at room temperature in air.  $Si_3N_4$  ceramic balls were adopted as the counterparts. The load was 10 N applied for 30 min, and the sliding speed was 3 mm/s. The morphologies and chemical compositions of the worn surfaces were analyzed by SEM and EDS. The wear volumes of both the substrate and the coatings were evaluated by a MT-500 surface profiler (Lanzhou Zhongke Kaihua Technology Development Co., Ltd., Lanzhou, China).

#### 2.4. High-Temperature Oxidation Tests

The coatings were cut into the cubes with a dimension of 5 mm × 4 mm × 1.5 mm, and their surfaces were ground with 600 and 1200 grit SiC abrasive papers in turn. Then the resultant coatings were placed in an OTF-1200X-80 electric furnace (Hefei Kejing Material Technology Co., Ltd., Hefei, China) for the isothermal oxidation tests. The tests were carried out in 1000 °C air for 120 h with a temperature accuracy of ± 0.5 °C. The weight gain of these samples was measured every hour throughout the test using a BSA124S analytical balance (Sartorius Scientific Instruments (Beijing) Co., Ltd., Beijing, China) with an accuracy of 0.1 mg. After the test, the oxidation film formed on the coating ( $Al_{1.5}MoNbTa$ ) was measured by an ESCALB 250Xi X-ray photoelectron spectrometer (Thermo Fisher Scientific, Waltham, MA, USA).

### 3. Results

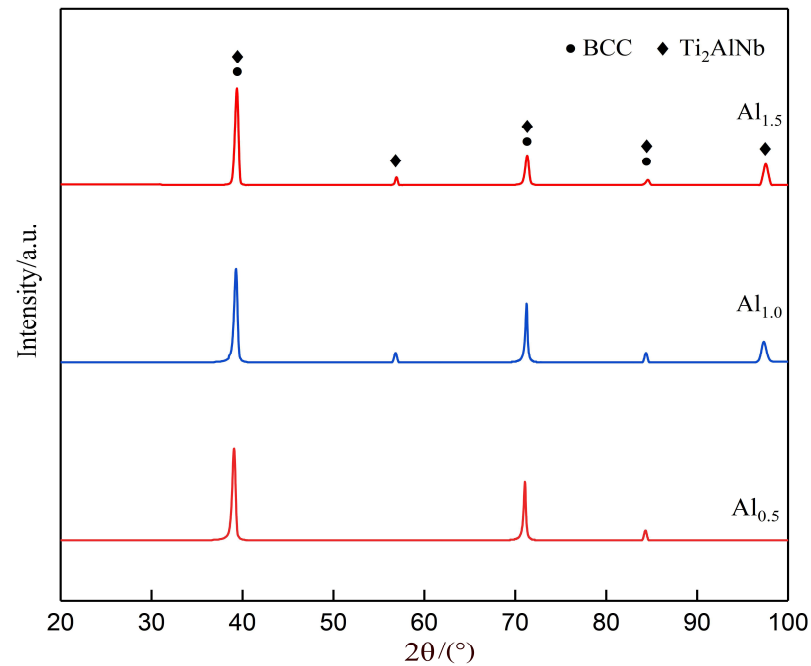
#### 3.1. Microstructural Characteristics

Figure 2 shows the XRD patterns of the coatings. The  $d$  values associated with all diffraction peaks match well with those in JCPDS cards (No. 00-089-3726 and No.00-049-1449). It implies that all the coatings consist of a solid solution with a BCC structure as the matrix phase and an intermetallic compound of  $Ti_2AlNb$  as the secondary phase. The high mixing entropy effect of HEAs contributes to the formation of disordered solid solutions by inhibiting the formation of intermetallic compounds [49]. However, the improvement in microhardness of RHEAs only containing single solid solutions is limited. Cai et al. [50] prepared a NiCrCoV HEA coating composed of BCC and FCC phases on Ti6Al4V by laser cladding. The microhardness was about 587.16 HV, which was only improved by approximately 80% than that of the substrate (325 HV). Ye et al. [51] fabricated the laser-clad  $Al_xFeCoNiCuCr$  RHEAs coatings with only BCC and FCC phases and the coatings exhibited the lower microhardness (about 538.5 HV<sub>0.2</sub>). With respect to the above-mentioned shortcomings, some ceramic particles (such as TiC, TiB<sub>2</sub>, TiN and NbC) were directly introduced into the HEA coatings to enhance their microhardness [52–56]. However, their surfaces easily suffer from contamination and the compatibility between ceramic particles and the matrix is usually poor [52–54]. In this study, we in situ synthesized  $Ti_2AlNb$  in the BCC matrix by designing the components of the cladding system. Park et al. [57] put forward a new method (called liquid phase separation) to predict the formed second phase in a multicomponent system, in which the elements with a negative mixing enthalpy ( $\Delta H_{mix}$ ) are subject to being separated from those with a positive value during solidification. Consequently, two different phases are formed. The  $\Delta H_{mix}$  values for each pair of elements were listed in Table 1 [58]. It is obvious that the three systems with respect to Al-Ti, Al-Nb and Al-Ta demonstrate the very negative values (−30, −18 and −19 KJ/mol<sup>−1</sup>), indicating that those binary alloys may be separated from the matrix. Nevertheless, the ternary system should be taken into account in this case since the mixing enthalpies of Al-Nb, Al-Ta and

Al-Ti are all nonpositive. The  $\Delta H_{\text{mix}}$  values of the ternary system formed among Al, Ti, Nb and Ta were calculated according to the following formula [59]:

$$\Delta H_{\text{mix}} = \sum_{i,j=1,i \neq j}^n \Omega_{ij} C_i C_j \quad (2)$$

where  $\Omega_{ij} = 4\Delta H_{\text{AB}}^{\text{mix}}$  is the interaction parameter;  $\Delta H_{\text{AB}}^{\text{mix}}$ , the mixing enthalpies (kJ/mol) of each pair the among Al, Ti, Nb and Ta, is given in Table 1 (noting that  $\Delta H_{\text{Nb,Ta}}^{\text{mix}} = 0$ );  $C_i$  and  $C_j$  signify the molar atom percentage of the  $i$  and  $j$  component.



**Figure 2.** X-ray diffraction patterns of  $\text{Al}_x\text{MoNbTa}$  RHEAs coatings.

**Table 1.** The mixing enthalpy ( $\Delta H_{\text{mix}}$ , KJ/mol) calculated for each pair of elements [58].

$\Delta H_{\text{mix}}$	Al	Mo	Nb	Ta	Ti
Al	-	-	-	-	-
Mo	-5	-	-	-	-
Nb	-18	-6	-	-	-
Ta	-19	-5	0	-	-
Ti	-30	-4	2	1	-

The results indicate that the values in the Al-Ti-Nb ( $-3.75$ ) is the most negative. Therefore, besides the matrix phase, the second phase containing Al-Ti-Nb ( $\text{Ti}_2\text{AlNb}$ ) is inclined to form in the given system ( $\text{Al}_x\text{MoNbTa}$ ), which is well in accordance with the XRD results. Besides, compared with the other elements, both Ta and Mo possess the higher melting point ( $T_{\text{Ta}} = 3290$  K,  $T_{\text{Mo}} = 2896$  K,  $T_{\text{Nb}} = 2750$  K,  $T_{\text{Ti}} = 1914$  K,  $T_{\text{Al}} = 933$  K). The zones rich in lower melting point elements (Al, Nb and Ti) become to solidify with a low speed, contributing to the formed precipitate separated from the liquid phase undergoing the rapid heating and cooling during laser cladding.

Careful inspection into XRD patterns reveals that there are two changes with the increase in Al content, corresponding to the slight increase in intensity of two diffraction peaks associated with  $\text{Ti}_2\text{AlNb}$  ( $2\theta = 57.69^\circ$  and  $97.67^\circ$ ), and the gradual deviation toward the right of a strong diffraction peak ( $2\theta = 39.05^\circ$ ). When  $x$  is increased from 0.5 to 1.0, two new diffraction peaks are observed at  $2\theta = 57.69^\circ$  and  $97.67^\circ$ , which can be indexed as  $\text{Ti}_2\text{AlNb}$ . Their intensity demonstrates the slight increase along increasing  $x$  to 1.5. The change indicates that the increase in Al content will be beneficial to the formation of

Ti<sub>2</sub>AlNb. On the other hand, the strongest peak moves from 39.05° to 39.37°, finally to 39.41° with  $x$  increased from 0.5 to 1.0, finally to 1.5, which means that the  $d$  value presents the downward tendency according to the Bragg equation ( $2d\sin\theta = \lambda$ ). The relative change in plane space ( $\Delta d/d_0$ ) was calculated to be 0.57% ( $x = 0.5$ ), 0.58% ( $x = 1.0$ ) and 0.61% ( $x = 1.5$ ), implying that an introduction of Al will aggravate the lattice distortion of the BCC matrix phase.

Figure 3 displays the SEM images of the middle zones in the cross sections of coatings with different  $x$  values. The microstructure of all coatings is very similar, which mainly consists of numerous white lath-like Ti<sub>2</sub>AlNb particles with a thickness of approximately 0.6  $\mu\text{m}$  and formless black BCC matrix. Close examination demonstrates that the area fraction of Ti<sub>2</sub>AlNb is gradually enhanced with the increase in  $x$  value, which is well consistent with that analyzed in XRD. The evolution in area fraction of Ti<sub>2</sub>AlNb with  $x$  was quantitatively analyzed by the analysis software named as image-pro plus 6.0. The area fraction of Ti<sub>2</sub>AlNb is improved from 42.6% ( $x = 0.5$ ) to 47.0% ( $x = 1.0$ ), and finally to 48.8% ( $x = 1.5$ ). The change will produce significant effects on the mechanical properties.

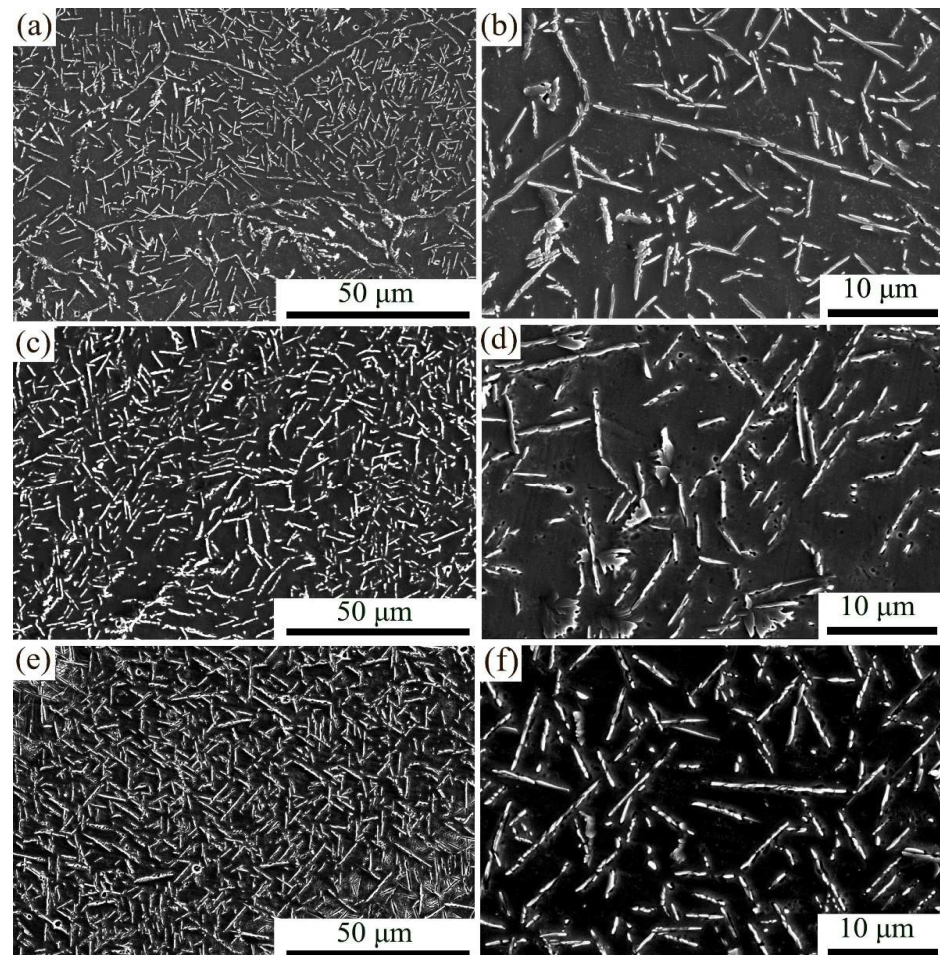


**Figure 3.** SEM images of the middle zones in the cross sections of coatings: (a,b) Al<sub>0.5</sub>, (c,d) Al<sub>1.0</sub>, (e,f) Al<sub>1.5</sub>.

### 3.2. Mechanical Properties

Figure 4 displays the microhardness profiles along the cross sections of the coatings. Given the change in microhardness value, the cross sections are broken up into two zones, namely the coating and the substrate. The microhardness of the coatings (687.60 HV<sub>0.2</sub>) is approximately 2 times that of the substrate (381.52 HV<sub>0.2</sub>). It implies that the resistance to micro-cutting of the substrate is enhanced by laser cladding the coatings on it. The coating can be subdivided into two zones, corresponding to the main strengthening zone with a

depth of 1.2 mm and the transition zone with a depth of 0.6 mm. The microhardness in the former is higher (719.02 HV<sub>0.2</sub> in average value) and fluctuates slightly in different zones, demonstrating that the microstructure in this zone is uniform. It can be clearly observed that the average microhardness is gradually improved in this zone with the increase in Al content (692.56 HV<sub>0.2</sub> for  $x = 0.5$ , 725.12 HV<sub>0.2</sub> for  $x = 1.0$  and 739.37 HV<sub>0.2</sub> for  $x = 1.5$ ). The phenomenon mainly depends on the increase in area fraction of Ti<sub>2</sub>AlNb and serious lattice distortion of BCC resulting from introducing more Al as analyzed in XRD and SEM. Ti<sub>2</sub>AlNb as an intermetallic compound may possess a higher microhardness than the BCC matrix. In order to clearly identify the difference in microhardness between Ti<sub>2</sub>AlNb and BCC, the Vickers indentations were prepared with a small applied load of 10 gf in the mixed zones containing BCC and Ti<sub>2</sub>AlNb (1–3) and the BCC zones (4–6) in the three coatings (Figure 5). The indentations can be prepared in the BCC zones due to their high area fraction and continuous distribution (4–6). However, it is very difficult to prepare the indentations in the Ti<sub>2</sub>AlNb particles due to their small size and discontinuous distribution. Therefore, the indentations were prepared in the mixed zones containing BCC and Ti<sub>2</sub>AlNb (1–3). By comparing the difference in microhardness between the BCC zone and the mixed zone of BCC+Ti<sub>2</sub>AlNb, the difference in microhardness between BCC and Ti<sub>2</sub>AlNb can be deduced. The tests should be carried out according to the Chinese standard (GB/T 4340.1-2009: Metallic materials-Vickers hardness test-Part 1: Test method), in which the distance between the two adjacent indentations should satisfy the requirements to obtain the precise value (the distance between adjacent indentation centers  $\geq 3$ –6 times diagonal length of the indentation). Based on above requirements, the data validity of every indentation shown in Figure 5 was verified. The results indicate that the data of Zones 1,3 in Figure 5a, Zones 1,2 in Figure 5b, and Zones 1, 2, 3, 4, 6 in Figure 5c are valid. The average microhardness values for the mixed zones containing BCC and Ti<sub>2</sub>AlNb, and the BCC zones are calculated of  $645.0 \pm 46.3$  HV<sub>0.01</sub> and  $567.6 \pm 30.9$  HV<sub>0.01</sub>, implying that the microhardness of Ti<sub>2</sub>AlNb is higher than that of BCC. Therefore, the increase in area fraction of Ti<sub>2</sub>AlNb with a higher microhardness plays an essential role in improving the microhardness of the coatings. Moreover, the microhardness the BCC matrix presents the slight upward tendency with increasing the Al content in the coatings (508.8 HV<sub>0.01</sub> for Al<sub>0.5</sub>, 558.3 HV<sub>0.01</sub> for Al<sub>1.0</sub> and 580.9 HV<sub>0.01</sub> for Al<sub>1.5</sub>), which is attributed to the more serious lattice distortion. Hence, the strengthening originating from the lattice distortion can be regarded as the other factor causing the increase in microhardness of the coatings. When the distance from the coatings' surfaces exceeds 1.2 mm, the microhardness shows a gradient distribution with a depth of 0.6 mm, which can be identified as the transition zone. The zone plays a significant buffering role in connecting the main strengthening zone and the soft substrate. When the coating is subjected to severe temperature difference or large external force, the debonding sensitivity of the coating can be reduced.

Besides the microhardness, the cracking susceptibility is regarded as the other index evaluating the performance of the coatings. The large residual stress is produced in the coatings due to the rapid heating and cooling characteristics of laser cladding, resulting in the high cracking susceptibility involved in the coatings. The morphologies of the indentations prepared in the middle of the coatings are exhibited in Figure 6, by which the values of  $a$  and  $c$  can be measured. Based on the Formula (1), the average values of fracture toughness ( $K_{IC}$ ) are calculated as follows: 3.935 MPa·m<sup>1/2</sup> for  $x = 0.5$ , 2.128 MPa·m<sup>1/2</sup> for  $x = 1.0$  and 1.717 MPa·m<sup>1/2</sup> for  $x = 1.5$ . It is clear that the increase in Al content will increase the cracking susceptibility of the coatings, which is associated with the increases in area fraction of Ti<sub>2</sub>AlNb and lattice distortion of BCC. The increase in cracking susceptibility will produce the negative role in wear resistance, which will promote the initiation and propagation of cracks and cause the brittle debonding of the coatings when subject to the long-term external force during sliding.

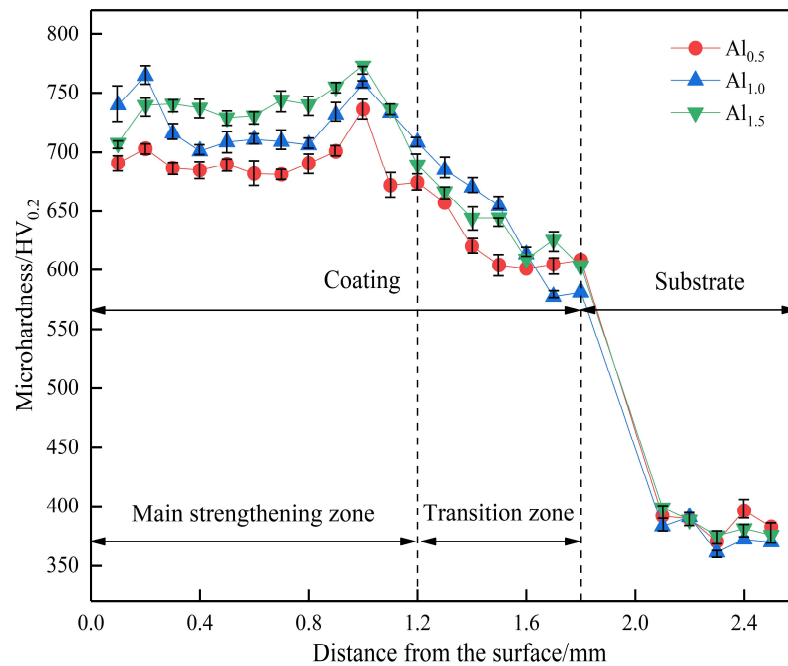


**Figure 4.** Microhardness distribution across the cross sections of the coatings.

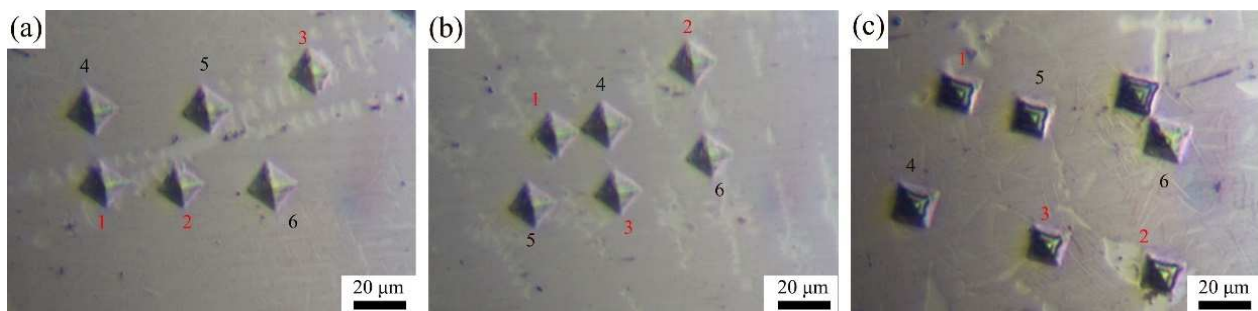


**Figure 5.** OM images of Vickers indentations prepared in the mixed zones containing BCC and  $Ti_2AlNb$  (1–3) and the BCC zones (4–6): (a)  $Al_{0.5}$ , (b)  $Al_{1.0}$  and (c)  $Al_{1.5}$ .

As shown in Figure 7, the coefficient of friction (hereafter denoted as COF) of the coatings and the substrate is plotted in detail as prolonging the sliding time. The COF values of the substrate fluctuate drastically with sliding time. Comparatively speaking, the values of coatings show a comparatively stable change along with time, and their average value is 59% that of the substrate. This indicates that the coatings possess a more superior antifriction performance than the substrate. In terms of the coatings, their COF values display a downward trend with the increase in  $x$  (0.49 for  $x = 0.5$ , 0.42 for  $x = 1.0$  and 0.35 for  $x = 1.5$ ), providing strong evidence that introducing more Al is favorable to the improvement in antifriction performance. For a given load ( $N$ ) applied to the samples, the high COF values mean that the large friction force is created between the friction pair during wear according to the formula ( $f = N$ ). For the soft substrate ( $Ti6Al4V$ ), the protrusions distributed on the hard counterpart can be easily impressed into the substrate surface under the given load, resulting in the significant increase in contacting area between the friction pairs. The counterpart will suffer from the great resistance (friction force) during sliding, resulting in a high COF obtained. Moreover, the protrusions impressed into the substrate surface may gravely change the surface morphology of the substrate since many furrows and bulges will be formed resulting from micro-cutting and severe deformation generated on substrate surface during wear. This implies that the surface states were considerably unstable, causing the drastic change in COF value. Comparatively speaking, the contacting

area between the counterpart and the coatings is small under the given load since the deformation resistance of the high microhardness coatings is enhanced, accompanied by which the COF value is reduced and fluctuates slightly with prolonging time.

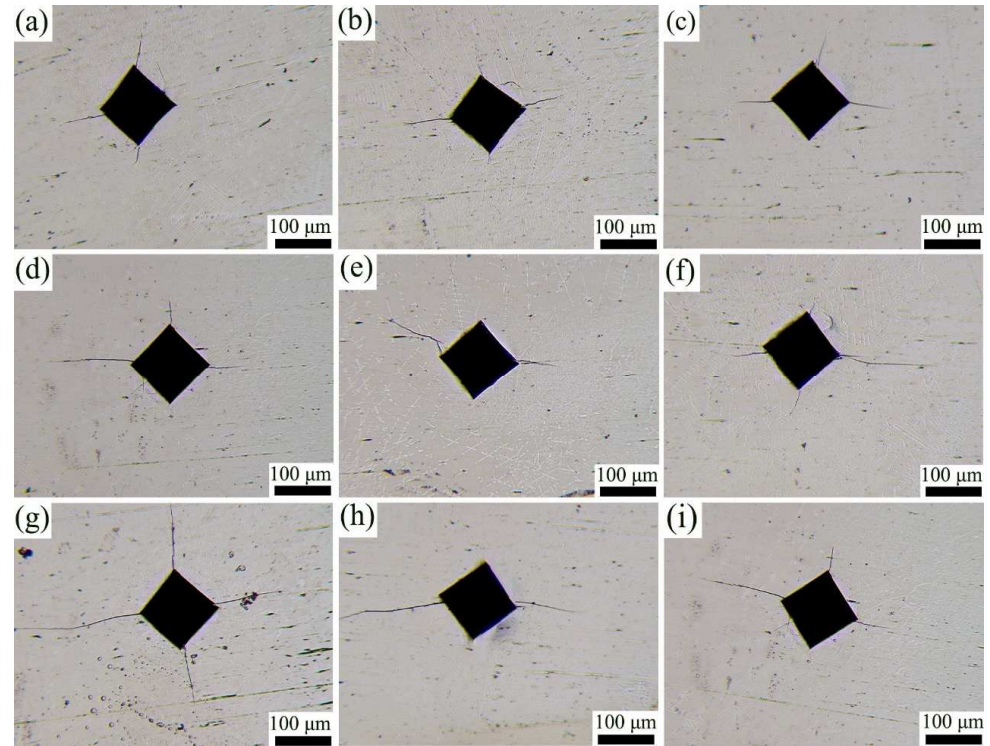


**Figure 6.** OM images of the Vickers indentations obtained in the middle zones with the same distance from the surface in the cross sections of coatings: (a–c)  $Al_{0.5}$ , (d–f)  $Al_{1.0}$ , and (g–i)  $Al_{1.5}$ .

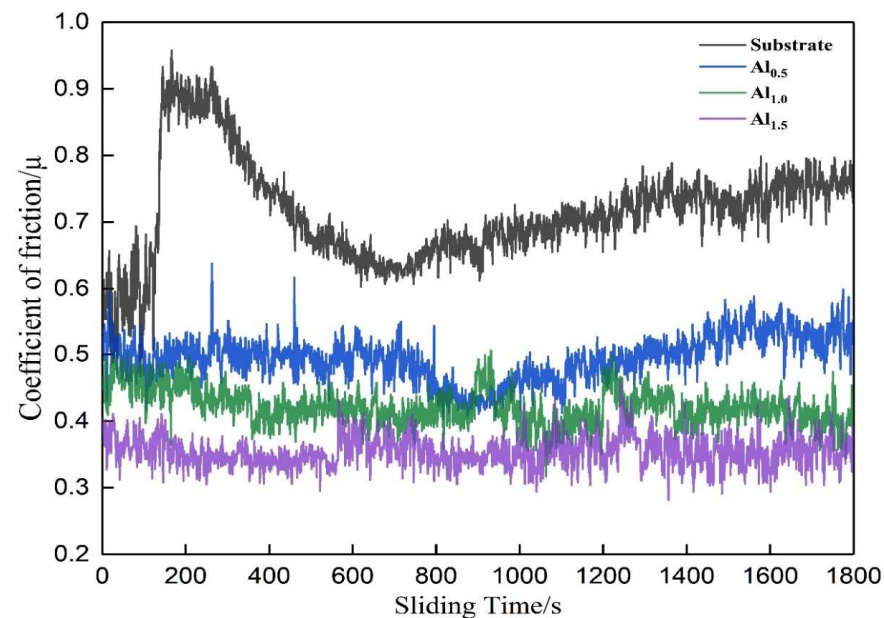


**Figure 7.** Coefficient of friction vs sliding time curves for the samples at room temperature under dry sliding wear test conditions.

Figure 8 displays overall worn morphologies of the substrate and the coating ( $x = 1.0$ ). Their widths are 2.12 mm (substrate) and 1.75 mm ( $x = 1.0$ ), respectively, which indicates the substrate undergoes more serious wear. Testing results of the volume loss ( $mm^3$ ) also confirm this (Figure 9). Figure 9b demonstrates the representative worn profiles of different

samples. The worn profiles were obtained by automatically moving the scanning probe with a slow speed of 0.3 mm/s and a high resolution of 0.02 μm. Based on the worn profiles, the corresponding volume losses can be automatically calculated by the surface profiler. The calculated results are shown in Figure 9a. Volume losses of the substrate and the coatings are  $1.78 \times 10^{-1} \text{ mm}^3$ ,  $0.34 \times 10^{-1} \text{ mm}^3$  ( $x = 0.5$ ),  $0.32 \times 10^{-1} \text{ mm}^3$  ( $x = 1.0$ ) and  $0.33 \times 10^{-1} \text{ mm}^3$  ( $x = 1.5$ ). The coatings demonstrate the similar volume losses, which is reduced by 81.45% when compared with that of the substrate. The wear rate (hereafter denoted as  $K$ ) can be calculated according to the following formula [60].

$$K = \frac{W}{SL} = \frac{W}{S_r T L} \tag{3}$$

where  $W$  is the volume loss of the sample ( $\text{mm}^3$ ),  $S$  represents the total sliding distance,  $S_r$  stands for the sliding speed (3 mm/s),  $T$  (s) denotes the whole sliding time, and  $L$  signifies the applied load (N).

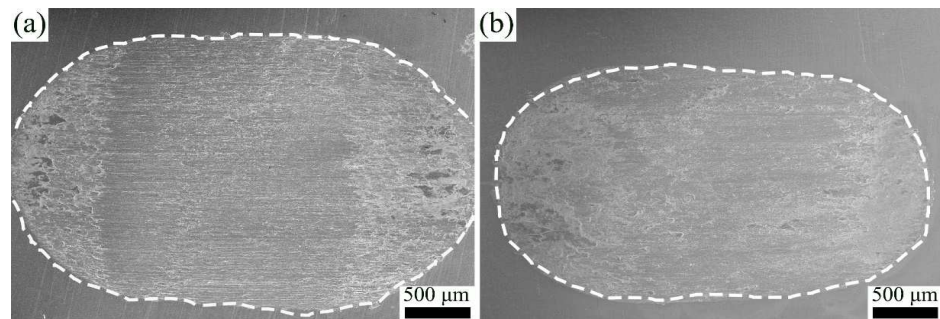


Figure 8. SEM images of worn surface morphologies of (a) the substrate (Ti6Al4V) and (b) the coating ( $\text{Al}_{1.0}$ ) at room temperature under dry sliding wear test conditions.

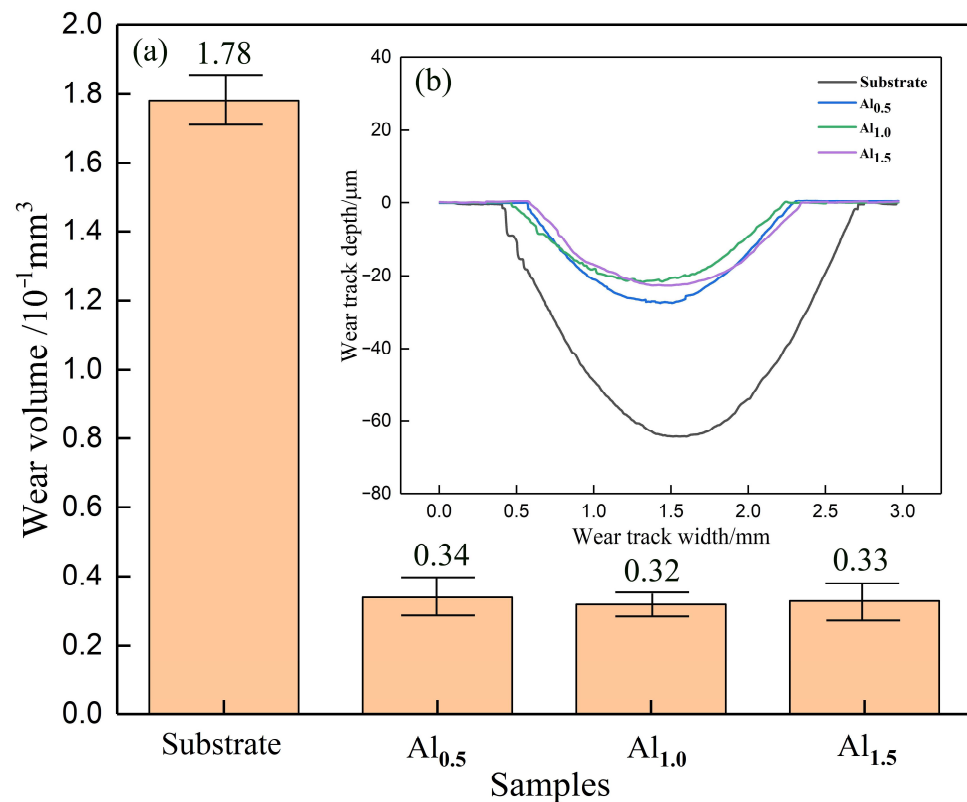


Figure 9. (a) Volume losses and (b) worn profiles tested by automatically moving the probe with a low speed of 0.3 mm/s and a high resolution of 0.02 μm.

The wear rates of the samples are  $3.31 \times 10^{-4}$  (substrate),  $6.34 \times 10^{-5}$  ( $x = 0.5$ ),  $5.90 \times 10^{-5}$  ( $x = 1.0$ ) and  $6.18 \times 10^{-5} \text{ mm}^3/\text{N}\cdot\text{m}$  ( $x = 1.5$ ). All of these coatings maintain a low level of wear rate. The wear rate of the coatings is first decreased, and then increased with increasing  $x$  value, resulting in the lowest value recorded in the coating with  $x = 1.0$ . This result originates from the combination effect of micro-cutting and brittle-debonding. With the increase in  $x$ , the resistance to micro-cutting presents the upward tendency due to the improvement in microhardness, which will cause the reduction in wear loss. However, the accompanied increase in cracking susceptibility will produce the opposite effect on wear loss, namely causing the increase in wear loss due to the brittle debonding. The opposite effects result in the lowest wear loss acquired in the coating ( $x = 1.0$ ).

Figure 10 displays SEM images of worn surface morphologies of the substrate and the coatings. As shown in Figure 10a, the worn surface of the substrate is considerably rough, on which some long grooves resulting from micro-cutting and deformation can be clearly observed. Moreover, a large number of fine debris particles are embedded into the surface, besides which the other particles cluster together and are crushed into small pieces of films to adhere to the surface. Figure 10b is the corresponding back scattering electron (BSE) image, from which the difference in atomic number among those zones can be clearly identified. It can be inferred that the zones covered with fine separated debris particles and small pieces of films should possess a lower atomic number than the other exposed zones since the former look darker. EDS was used to identify chemical compositions in different zones. The results are listed in Table 2. The two zones (Zones 1 and 2) are composed of Al, Ti, V and O, indicating that initial metallic elements involved in the substrate suffer from the oxidation under the action of generated friction during sliding. However, the dark grey zones composed of separated or clustered debris particles contain a higher content of O (48.79 at.%), which is approximately triple that of the other exposed zones (15.93 at.%). The fine debris particles exfoliating from the substrate surface possess a high specific surface energy, and their mechanical behaviors are fairly complicated during wear, resulting in the more severe oxidation occurring on them. The sharp separated debris particles may continually move on the substrate surface during sliding and further generate the micro-cutting on it. However, the blunt particles may be embedded into the substrate surface and cause the fatigue failure. Different from the above-mentioned negative effects in wear resistance from the separated particles, the small pieces of films containing clustered particles undergoing the deformation will shield the substrate surface from destruction. Therefore, the wear mechanism can be identified as the mixture wear of serious micro-cutting and oxidation. For the coating with  $x = 0.5$ , a small number of slight micro-cutting patterns and some large pieces of films in Figure 10c are clearly observed on the worn surface. The corresponding BSE image is shown in Figure 10d, in which the pieces of film are darker than the other zones. EDS results also indicate that the whole worn surface (Zones 3 and 4) is also oxidized during sliding at room temperature (Table 2). However, the O content involved in the films is also higher than that in the other zones, which is similar to that obtained in the substrate. By a close comparison in worn morphology between the substrate and the coating with  $x = 0.5$ , it can be concluded that the coating demonstrates more excellent wear resistance due to slighter micro-cutting and stronger protection from huge films. The enhancement in microhardness of the coating should be responsible for the improvement in wear resistance. On the one hand, the high microhardness will endow the coating with excellent deformation resistance, causing the improvement in micro-cutting resistance. Moreover, the high microhardness makes the debonding debris particles difficultly embedded into the coating, so that they can freely move on the coating surface during sliding and more easily cluster to form large pieces of films with a stronger protection role. The wear mechanism of the coating is transformed into slight micro-cutting and oxidation, when compared with that of the substrate. The worn morphology of the coating with  $x = 1.0$  is similar to that with  $x = 1.5$  (Figure 10e,f for  $x = 1.0$ , Figure 10g,h for  $x = 1.5$ ). As shown in Table 2, the chemical compositions for the zones with different contrasts were analyzed by EDS (Zones 5 and 6 in Figure 10f and

Zones 7 and 8 in Figure 10h), showing that the whole worn surfaces suffer from different degrees of oxidation. A close examination reveals that the edge of the covered oxidation film has broken into numerous fragments in Figure 10g, besides which some fine cracks are also observed on the film surface. This indicates that the film ( $x = 1.5$ ) possesses the higher cracking susceptibility when compared with that ( $x = 1.0$ ) due to a higher area fraction of  $Ti_2AlNb$  and a more serious lattice distortion in BCC involved in the former. This is also well consistent with the above-mentioned testing results of fracture toughness ( $3.935 \text{ MPa}\cdot\text{m}^{1/2}$  for  $x = 0.5$ ,  $2.128 \text{ MPa}\cdot\text{m}^{1/2}$  for  $x = 1.0$ ,  $1.717 \text{ MPa}\cdot\text{m}^{1/2}$  for  $x = 1.5$ ). The film with a high cracking susceptibility suffers from severe destruction, resulting in the protective effect for the coating weakened to a certain extent. Consequently, the wear rate of the coating ( $x = 1.5$ ) is slightly higher than that ( $x = 1.0$ ). Therefore, the wear mechanism of the coating ( $x = 1.5$ ) can be determined as the combination of slight micro-cutting, oxidation and brittle debonding.

### 3.3. Oxidation Behaviors

Figure 11 displays the mass change per area versus time for the substrate and the coatings undergoing the oxidation at  $1000 \text{ }^\circ\text{C}$  up to 120 h. For all the samples, the oxidation process can be divided into two stages, corresponding to the serious oxidation stage and the stable oxidation stage. In the former, the sample surface is directly exposed to the air and subject to oxidation at a high rate, causing the drastic increase in mass gain. Accompanied with oxidation, a thin oxidation film is formed on the substrate and acts as a barrier to greatly retard the oxygen into the substrate, resulting in the slow mass gain and prolonging the time. It can be seen that the serious oxidation stage of the substrate lasts for approximately 35 h, which is longer than that of the coatings (22 h). Moreover, the resultant mass gain of the coatings after 120 h is reduced by approximately 50% when compared with that of the substrate ( $120.3 \text{ mg}/\text{cm}^2$  for the substrate and  $58.6 \text{ mg}/\text{cm}^2$  for the coatings). The results indicate that the dense oxidation film is easily formed on the coatings' surfaces and demonstrates stronger resistance to oxygen invasion. Namely, the oxidation resistance of the substrate can be improved by laser cladding the RHEAs coatings on it. With respect to the coatings, the resultant mass gain presents the slight downward tendency with increasing the Al content ( $61.8 \text{ mg}/\text{cm}^2$  for  $x = 0.5$ ,  $57.8 \text{ mg}/\text{cm}^2$  for  $x = 1.0$ ,  $56.3 \text{ mg}/\text{cm}^2$  for  $x = 1.5$ ), which means that the introduction of Al contributes to the improvement in oxidation resistance to a certain extent.

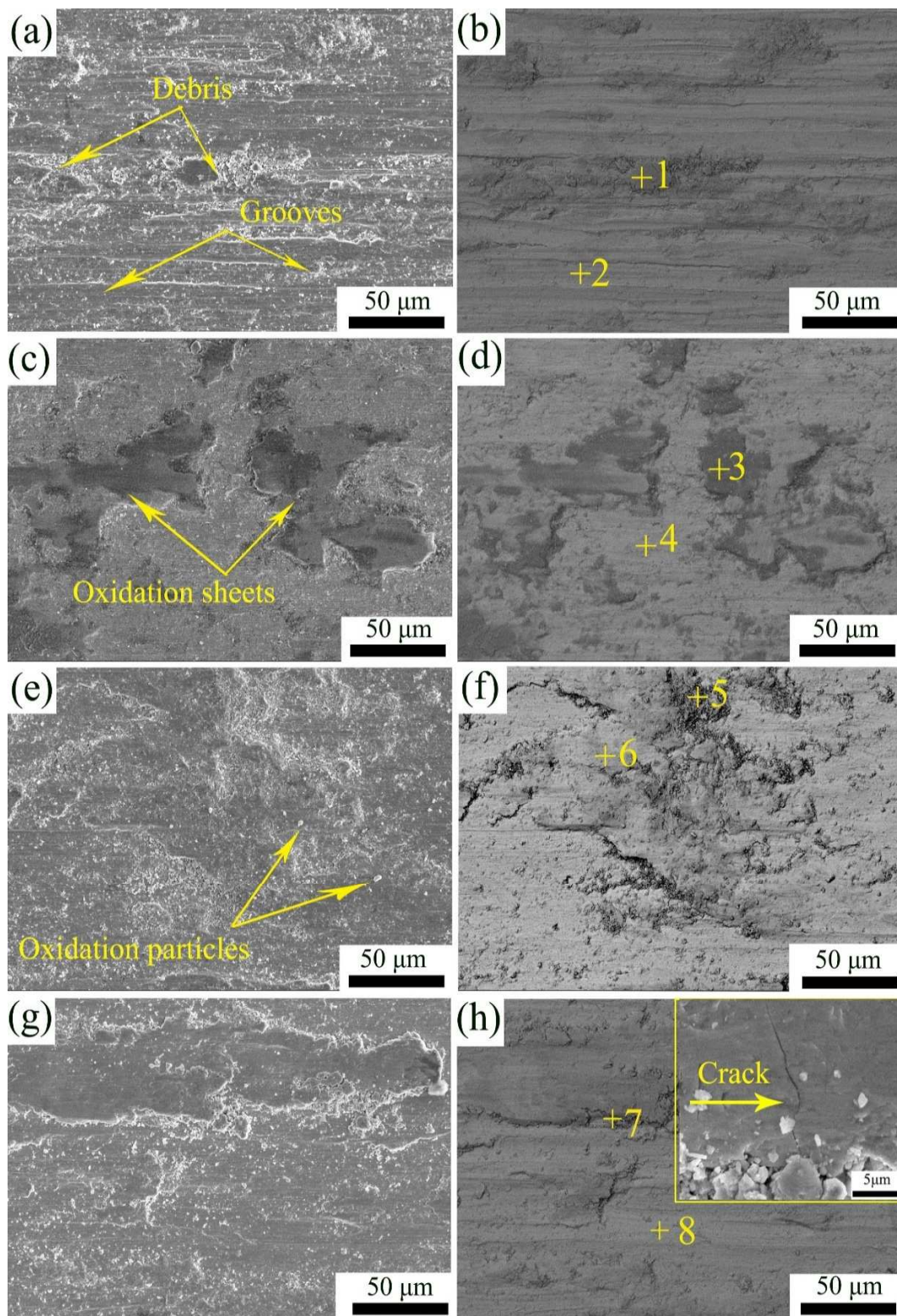
The relationship between mass gain and time can be well fitted into the linear function for the serious oxidation and the parabolic function for the stable oxidation. The two functions can be expressed as follows:

$$m = K_1(t + b) \text{ for the serious oxidation stage} \quad (4)$$

$$(m + a) = K_2(t + b)^2 \text{ for the stable oxidation stage} \quad (5)$$

where  $m$  denotes the mass gain (mg),  $t$  represents the oxidation time (h),  $K_1$  and  $K_2$  signify the oxidation rate at the two stages,  $a$  and  $b$  stand for the constants.

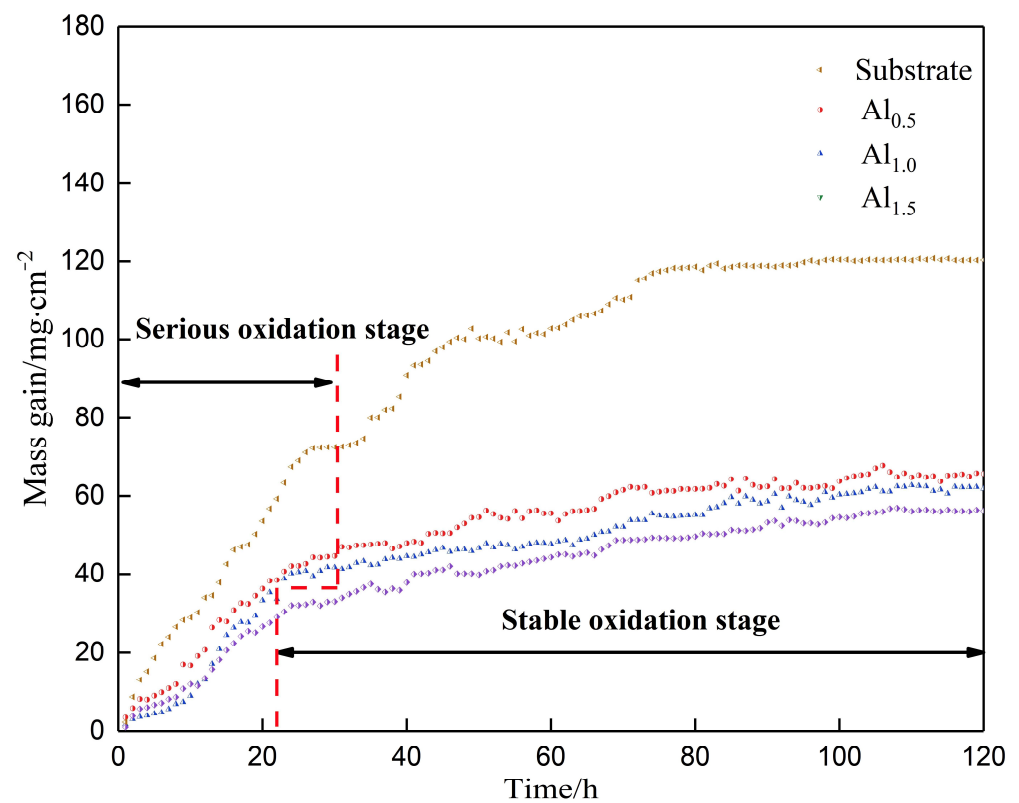
The fitting results are displayed in Figure 12 and Table 3. The coefficient of determination (COD) was calculated to evaluate the fitting degree ( $R_1^2$  represents the COD at the serious oxidation stage and  $R_2^2$  stands for the COD at the stable oxidation stage). The results demonstrate that all values are close to 1, indicating the high fitting degree acquired.



**Figure 10.** SEM images of worn surface morphologies of (a,b) substrate (Ti6Al4V) and (c,d) Al<sub>0.5</sub>, (e,f) Al<sub>1.0</sub> and (g,h) Al<sub>1.5</sub> subject to the dry-sliding reciprocating wear testing at room temperature in air (Si<sub>3</sub>N<sub>4</sub> as the counterparts, the 10 N load for 30 min, and the 3 mm/s sliding speed).

**Table 2.** Chemical compositions (precision of 1–5%) of the zones on the worn surfaces of the substrate and the coatings marked in Figure 10.

Samples	Zones	Chemical Compositions (at.%)						
		O	Al	Nb	Mo	Ti	Ta	V
Substrate	1	48.79	06.08	-	-	43.21	-	01.92
	2	15.93	09.55	-	-	71.90	-	02.62
Al <sub>0.5</sub>	3	35.99	4.4	5.85	6.04	38.87	8.85	-
	4	21.92	5.29	7.99	7.5	46.85	10.44	-
Al <sub>1.0</sub>	5	44.28	6.19	3.52	3.47	37.1	5.44	-
	6	38.35	7.68	3.95	4.14	40.57	5.31	-
Al <sub>1.5</sub>	7	34.96	10.94	3.2	3.23	41.85	5.81	-
	8	18.44	9.77	5.57	5.39	52.52	8.31	-

**Figure 11.** Oxidation mass gain curves of the substrate and the coatings after exposed to 1000 °C in air for 120 h.

The difference in oxidation resistance of the samples mainly depends on the formation preference of oxidation films and its densification. In order to reveal the formation mechanism of oxidation films, XPS was applied to detect chemical compositions of oxidation films and chemical valence states of alloying elements. Figure 13a shows the survey spectrum of the RHEAs coating (Al<sub>1.5</sub>) subject to oxidation, which verifies that Al, Mo, Nb, Ta and Ti in the coating are transformed into oxides. For the Al<sub>2p</sub> spectrum (Figure 13b), a strong peak is observed at 73.83 eV, which originates from the existence of Al<sub>2</sub>O<sub>3</sub>. The Mo<sub>3d</sub> spectrum is composed of three peaks with the binding energies of 229.03 eV, 231.68 eV and 235.43 eV (Figure 13c), implying the existence of MoO<sub>2</sub> and MoO<sub>3</sub>. It should be pointed out that MoO<sub>2</sub> is unstable and is not taken into consideration in many studies [61]. With respect to the Nb<sub>3d</sub> spectrum, two strong peaks situated at 206.28 eV and 209.13 eV can be identified

(Figure 13d), which are related to the existence of  $\text{Nb}_2\text{O}_5$ . For the  $\text{Ta}_{4f}$  spectrum (Figure 13e), two asymmetric peaks associated with  $\text{Ta}_2\text{O}_5$  are observed at 25.23 eV and 27.08 eV, while loss features, referred to as Ta metal and  $\text{Ta}_2\text{O}_5$ , can be observed at 30.08 and 37.03 eV as a result of the inelastic collision energy loss in photoelectron through the surface atoms (Ta) or molecules ( $\text{Ta}_2\text{O}_5$ ). For the  $\text{Ti}_{2p}$  spectrum (Figure 13f), two asymmetric peaks observed at 458.03 and 464.13 eV confirm the formation of  $\text{TiO}_2$ , besides which a small satellite features peak can be found at 472.03 eV.

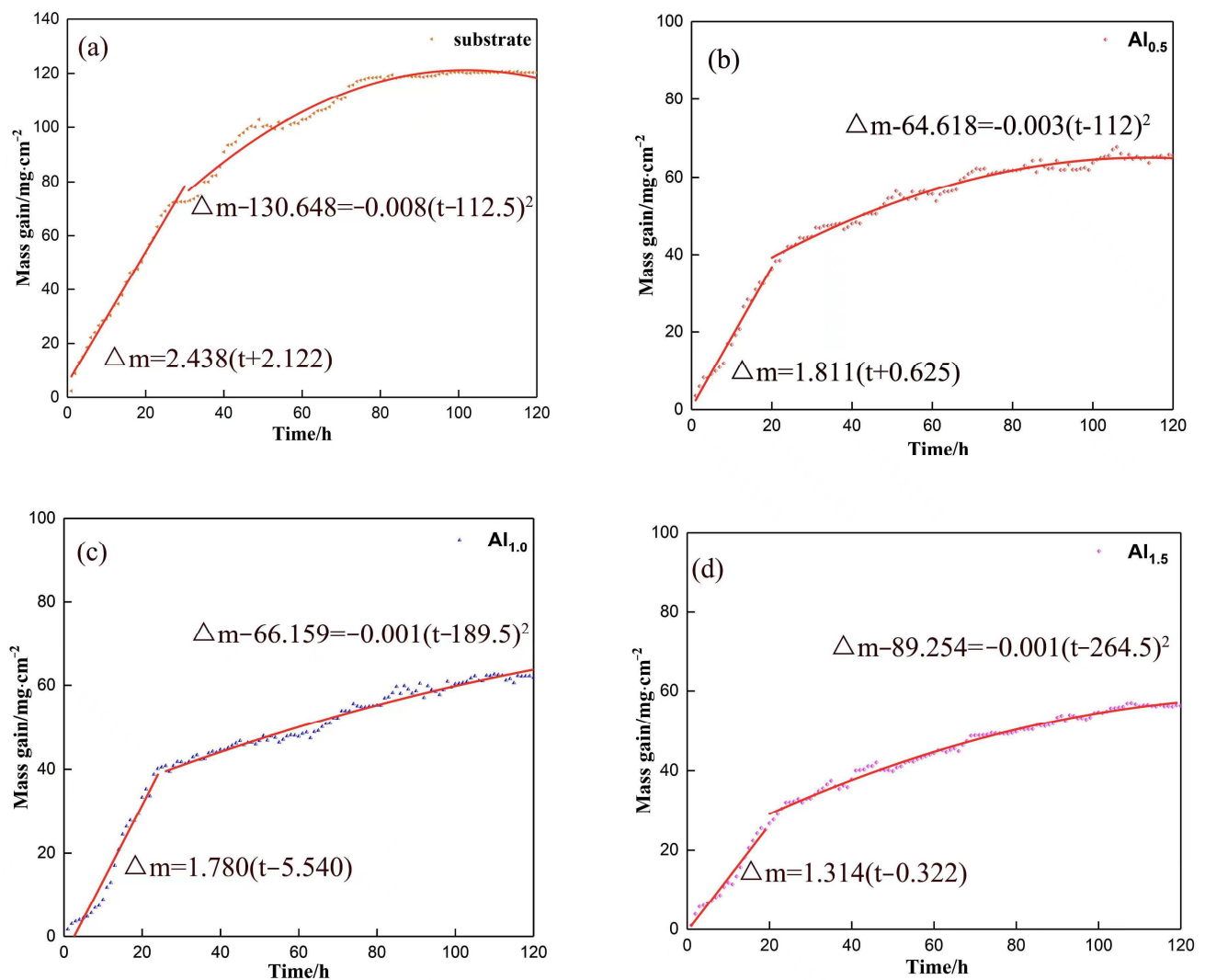


**Figure 12.** Oxidation mass gain fitting curves of the substrate and the coatings after exposed to 1000 °C in air for 120 h: (a) substrate, (b)  $\text{Al}_{0.5}$ , (c)  $\text{Al}_{1.0}$  and (d)  $\text{Al}_{1.5}$ .

**Table 3.** The calculated parameters according to the fitting curves shown in Figure 12.

Samples	Serious Oxidation Stage			Stable Oxidation Stage			
	$K_1$ (mg/h)	$a$ (mg)	$\text{COD}(R_1^2)$	$K_2$ (mg/h <sup>2</sup> )	$a$ (mg)	$b$ (h)	$\text{COD}(R_2^2)$
Substrate	2.438	2.122	0.99	−0.008	−130.648	−112.5	0.96
$\text{Al}_{0.5}$	1.811	0.625	0.98	−0.003	−64.618	−112.0	0.98
$\text{Al}_{1.0}$	1.780	−5.540	0.96	−0.001	−66.159	−189.5	0.97
$\text{Al}_{1.5}$	1.314	−0.322	0.96	−0.001	−89.254	−264.5	0.99

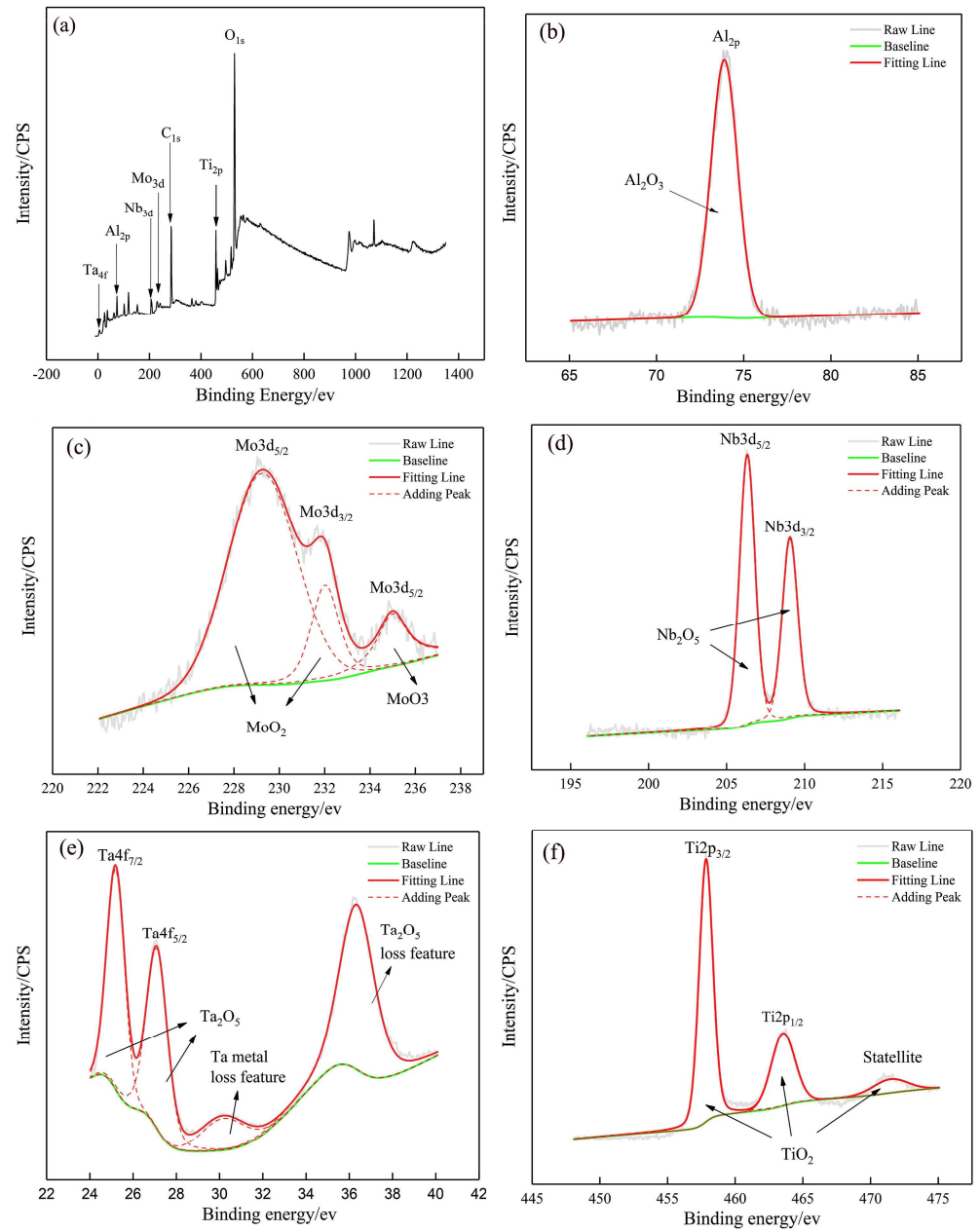


**Figure 13.** XPS spectra for the oxide film on the surface of the coating with  $x = 1.5$  after exposed to  $1000\text{ }^{\circ}\text{C}$  in air for 120 h: (a) survey spectrum, (b)  $\text{Al}_{2p}$  spectrum, (c)  $\text{Mo}_{3d}$  spectrum, (d)  $\text{Nb}_{3d}$  spectrum, (e)  $\text{Ta}_{4f}$  spectrum and (f)  $\text{Ti}_{2p}$  spectrum.

Based on the XPS results, it can be concluded that the following reactions occur during oxidation.



The occurring preference of the above-mentioned reactions can be evaluated by the thermodynamic calculation. As shown in Figure 14, the changes in standard Gibbs free

energy ( $\Delta G$ ) of those reactions are negative in a wide temperature range from 298 K to 1400 K, indicating that all reactions can occur spontaneously. In the given oxidation temperature (1273.15 K in Figure 14), the formation priority of oxides follows the order as  $Ta_2O_5 > Nb_2O_5 > Al_2O_3 > MoO_3 > TiO_2$ . Those preferentially formed oxidation films ( $Ta_2O_5$ ,  $Nb_2O_5$ ) can act as a first barrier to retard the oxygen into the coatings, which result in the mass gain of the coatings reduced when compared with that of the substrate without Ta and Nb. From the point of thermodynamics, the difference in oxidation resistance between the coatings and the substrate can be explained; however, this cannot be explained among the three coatings.

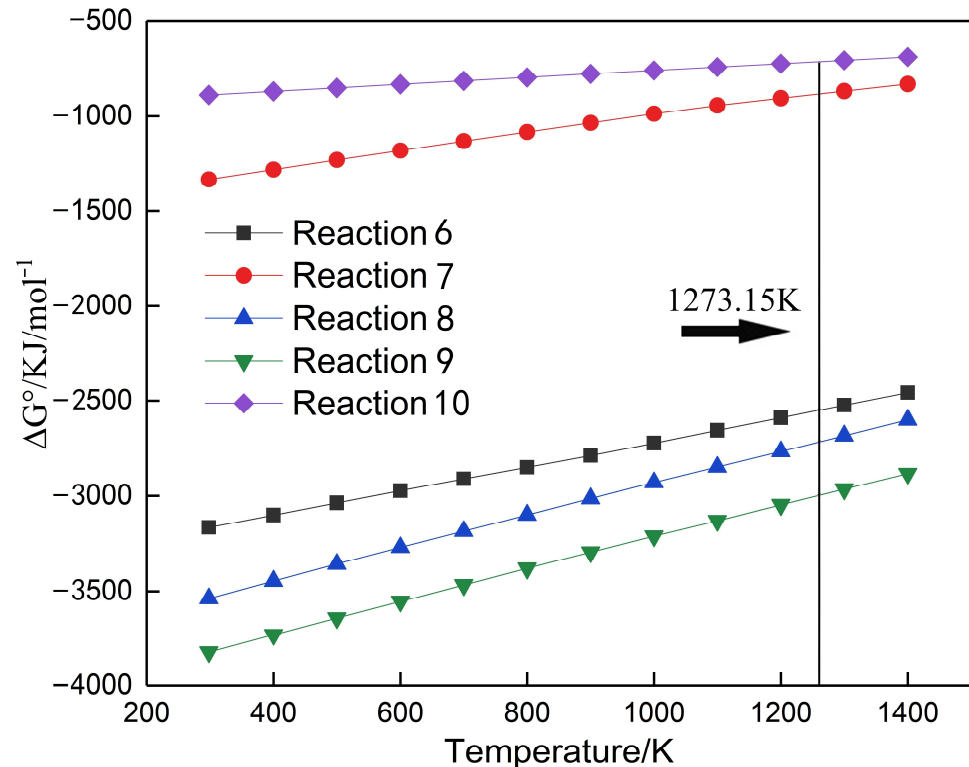


**Figure 14.** The relationship between temperature and the standard Gibbs free energy of reactions (6)–(10).

Besides the occurring preference of oxidation reactions, the densification of the formed oxidation films can be regarded as the other essential factor responsible for the oxidation resistance. The densification can be assessed by the Pilling Bedworth ratio (PBR), manifesting the volume change of a specific substance before and after oxidation. For an alloying component (A) subject to oxidation ( $2mA + nO_2 \rightarrow 2A_mO_n$ ), the PBR value can be calculated [62].

$$PBR = \frac{V_{A_mO_n}}{mV_A} = \frac{M_{A_mO_n}\rho_A}{m\rho_{A_mO_n}M_A} \quad (11)$$

where  $V_{A_mO_n}$  represents the relative molecular volume of metal oxides, and  $V_A$  denotes the relative molecular volume of metal.  $m$  stands the mole number of substances involved in the oxidation reaction.  $M_{A_mO_n}$  is the relative molecular weight of oxides, and  $M_A$  is the relative molecular weight of metal.  $\rho_{A_mO_n}$  represents the density of oxides, and  $\rho_A$  stands for the density of metal.

According to the above Formula (11), the PBR values for Reactions (6)–(10) can be calculated as 1.28, 3.29, 2.68, 2.50 and 1.70. When the value is less than 1, a discontinuous and porous oxide film is formed on the metal surface, which cannot efficiently block the oxygen from invading the metal. On the contrary, a PBR value larger than 1 means that the metal will be covered with a continuous and dense oxide film and undergo the weak

oxidation. However, an excessively high value ( $>2$ ) will imply that high internal stress will be generated in oxidation films and possibly result in the initiation and propagation of cracks, aggravating the oxidation due to the oxidation film easily debonding from the metal surface. The more introduction of Al contributes to reduce the internal stress due to their comparatively low PBR value, causing the slight reduction in mass gain of the coatings.

Regarding to the comprehensive effect of Al on wear resistance and high temperature oxidation of the coatings, the suitable introduction content of Al can be ascertained as  $x = 1.0$ .

#### 4. Conclusions

(1) The RHEAs coatings were synthesized on Ti6Al4V by laser cladding to improve its wear resistance and high temperature oxidation resistance, in which an intermetallic compound of  $Ti_2AlNb$  as the secondary phase and a BCC phase was contained. Introducing more Al in the coatings resulted in the increase in area fraction of  $Ti_2AlNb$  and lattice distortion of BCC.

(2) The increase in Al content caused the increase in microhardness of the coatings (692.56  $HV_{0.2}$  for  $x = 0.5$ , 725.12  $HV_{0.2}$  for  $x = 1.0$  and 739.37  $HV_{0.2}$  for  $x = 1.5$ ), accompanied by which their fracture toughness was correspondingly reduced (3.935  $MPa \cdot m^{1/2}$  for  $x = 0.5$ , 2.128  $MPa \cdot m^{1/2}$  for  $x = 1.0$  and 1.717  $MPa \cdot m^{1/2}$  for  $x = 1.5$ ). The two changes produced the opposite effects on wear loss. The comprehensive effects resulted in the lowest wear loss obtained in  $x = 1.0$ , which was reduced by approximately 82.18% when compared with that of the substrate.

(3) The increase in Al content contributed to the improvement in oxidation resistance of the coatings due to the oxidation gain mass of the coatings subject to oxidation at 1000 °C for 120 h gradually reduced (61.8  $mg/cm^2$  for  $x = 0.5$ , 57.8  $mg/cm^2$  for  $x = 1.0$  and 56.3  $mg/cm^2$  for  $x = 1.5$ ). The change was associated with the enhancement in the oxidation film owing to Al with a comparatively low PBR value.

(4) The suitable introduction content of Al was ascertained as  $x = 1.0$  regarding to both wear resistance and high temperature oxidation resistance.

**Author Contributions:** Investigation, experiment, formal analysis, writing—original draft, S.H.; resources, supervision, methodology, J.L.; experiment, formal analysis, validation, P.Z., Y.X. and W.L. All authors have read and agreed to the published version of the manuscript.

**Funding:** This research was funded by the National Natural Science Foundation of China, Grant No.51471105, and Natural Science Foundation of Shanghai, Grant No. 20ZR142200.

**Institutional Review Board Statement:** Not applicable.

**Informed Consent Statement:** Not applicable.

**Data Availability Statement:** Not applicable.

**Conflicts of Interest:** The authors declare no conflict of interest.

#### References

1. Liu, Y.N.; Yang, L.J.; Yang, X.J.; Zhang, T.G.; Sun, R.L. Optimization of microstructure and properties of composite coatings by laser cladding on titanium alloy. *Ceram. Int.* **2021**, *47*, 2230–2243. [[CrossRef](#)]
2. Gurrappa, I. Characterization of titanium alloy Ti6Al4V for chemical, marine and industrial applications. *Mater. Charact.* **2003**, *51*, 131–139. [[CrossRef](#)]
3. Zhou, H.Y.; Shi, X.L.; Lu, G.C.; Chen, Y.; Yang, Z.Y.; Wu, C.H.; Xue, Y.W.; Ibrahim, A.M.M. Friction and wear behaviors of Ti6Al4V alloy with surface microporous channels filled by Sn-Ag-Cu and  $Al_2O_3$  nanoparticles. *Surf. Coat. Technol.* **2020**, 387. [[CrossRef](#)]
4. Liang, J.; Liu, X.B.; Ke, J.; Luo, Y.S.; Liang, L. Preparation and high temperature oxidation resistance of laser deposited  $Ti_5Si_3/MoSi_2/Mo_5Si_3$  reinforced  $\alpha$ -Ti/NiTi composite coatings. *Surf. Coat. Technol.* **2019**, *372*, 56–64. [[CrossRef](#)]
5. Cui, Y.H.; Hu, Z.C.; Ma, Y.D.; Yang, Y.; Zhao, C.C.; Ran, Y.T.; Gao, P.Y.; Wang, L.; Dong, Y.C.; Yan, D.R. Porous nanostructured  $ZrO_2$  coatings prepared by plasma spraying. *Surf. Coat. Technol.* **2019**, *363*, 112–119. [[CrossRef](#)]
6. Li, X.F.; Wei, Z.S.; Zuo, D.W.; Wang, M. Corrosion Resistance of TC4 Alloy Implanted by La+, Mo+. *Key Eng. Mater.* **2006**, *315*, 61–65. [[CrossRef](#)]

7. Zhang, W.G.; Liu, W.M.; Liu, Y.; Wang, C.T. Tribological behaviors of single and dual sol–gel ceramic films on Ti6Al4V. *Ceram. Int.* **2009**, *35*, 1513–1520. [[CrossRef](#)]
8. Xie, R.Z.; Lin, N.M.; Zhou, P.; Zou, J.J.; Han, P.J.; Wang, Z.H.; Tang, B. Surface damage mitigation of TC4 alloy via micro arc oxidation for oil and gas exploitation application: Characterizations of microstructure and evaluations on surface performance. *Appl. Surf. Sci.* **2018**, *436*, 467–476. [[CrossRef](#)]
9. Das, A.; Shukla, M. New generation hopeite coating on Ti6Al4V (TC4) by radio frequency magnetron sputtering for prosthetic-orthopaedic implant applications: Synthesis and characterisation. *Trans. IMF* **2020**, *98*, 88–96. [[CrossRef](#)]
10. Zhang, Q.; Liang, Z.L.; Cao, M.; Liu, Z.F.; Zhang, A.F.; Lu, B.H. Microstructure and mechanical properties of Ti6Al4V alloy prepared by selective laser melting combined with precision forging. *Trans. Nonferrous Met. Soc. China* **2017**, *27*, 1036–1042. [[CrossRef](#)]
11. Yue, T.M.; Xie, H.; Lin, X.; Yang, H.O.; Meng, G.H. Solidification behavior in laser cladding of AlCoCrCuFeNi high-entropy alloy on magnesium substrates. *J. Alloys Compd.* **2014**, *587*, 588–593. [[CrossRef](#)]
12. Leyens, C.; Beyer, E. 8-Innovations in laser cladding and direct laser metal deposition. *Surf. Eng.* **2015**, 181–192. [[CrossRef](#)]
13. Song, J.L.; Li, Y.T.; Deng, Q.L.; Hu, D.J. Research Progress of Laser Cladding Forming Technology. *J. Mech. Eng.* **2010**, *46*, 29–39. [[CrossRef](#)]
14. Sun, R.L.; Lei, Y.W.; Niu, W. Laser clad TiC reinforced NiCrBSi composite coatings on Ti6Al4V alloy using a CW CO<sub>2</sub> laser. *Surf. Coat. Technol.* **2009**, *203*, 1395–1399. [[CrossRef](#)]
15. Li, N.; Xiong, Y.; Xiong, H.P.; Shi, G.Q.; Blackburn, J.; Liu, W.; Qin, R.Y. Microstructure, formation mechanism and property characterization of Ti+SiC laser clad coatings on Ti6Al4V alloy. *Mater. Charact.* **2018**, *148*, 43–51. [[CrossRef](#)]
16. Lv, Y.H.; Li, J.; Tao, Y.F.; Hu, L.F. High-temperature wear and oxidation behaviors of TiNi/Ti<sub>2</sub>Ni matrix composite coatings with TaC addition prepared on Ti6Al4V by laser cladding. *Appl. Surf. Sci.* **2017**, *402*, 478–494. [[CrossRef](#)]
17. Zhang, T.G.; Zhuang, H.F.; Zhang, Q.; Yao, B.; Yang, F. Influence of Y<sub>2</sub>O<sub>3</sub> on the microstructure and tribological properties of Ti-based wear-resistant laser-clad layers on TC4 alloy. *Ceram. Int.* **2020**, *46*, 13711–13723. [[CrossRef](#)]
18. Zhuang, Q.Q.; Zhang, P.L.; Li, M.C.; Yan, H.; Yu, Z.S.; Lu, Q.H. Microstructure, Wear Resistance and Oxidation Behavior of Ni-Ti-Si Coatings Fabricated on Ti6Al4V by Laser Cladding. *Materials* **2017**, *10*, 1248. [[CrossRef](#)]
19. Yeh, J.W.; Chen, S.K.; Lin, S.J.; Gan, J.Y.; Chin, T.S.; Shun, T.T.; Tsau, C.H.; Chang, S.Y. Nanostructured high-entropy alloys with multiple principal elements: Novel alloy design concepts and outcomes. *Adv. Eng. Mater.* **2004**, *6*, 299–303. [[CrossRef](#)]
20. Chen, G.; Li, L.T.; Qiao, J.W.; Jiao, Z.M.; Ma, S.G.; Ng, F.L.; Zhu, Z.G.; Zhao, D.; Wang, Z.H. Gradient hierarchical grain structures of Al<sub>0.1</sub>CoCrFeNi high-entropy alloys through dynamic torsion. *Mater. Lett.* **2019**, *238*, 163–166. [[CrossRef](#)]
21. Hua, N.B.; Wang, W.J.; Wang, Q.T.; Ye, Y.X.; Lin, S.H.; Zhang, L.; Guo, Q.H.; Brechtel, J.; Liaw, P.K. Mechanical, corrosion, and wear properties of biomedical Ti–Zr–Nb–Ta–Mo high entropy alloys. *J. Alloys Compd.* **2021**, *861*, 157997. [[CrossRef](#)]
22. Wang, Y.K.; Xie, Z.M.; Wang, M.M.; Deng, H.W.; Yang, J.F.; Jiang, Y.; Zhang, T.; Wang, X.P.; Fang, Q.F.; Liu, C.S. The superior thermal stability and tensile properties of hot rolled W–HfC alloys. *Int. J. Refract. Hard Met.* **2019**, *81*, 42–48. [[CrossRef](#)]
23. Nong, Z.S.; Lei, Y.N.; Zhu, J.C. Wear and oxidation resistances of AlCrFeNiTi-based high entropy alloys. *Intermetallics* **2018**, *101*, 144–151. [[CrossRef](#)]
24. Ding, Z.Y.; Cao, B.X.; Luan, J.H.; Jiao, Z.B. Synergistic effects of Al and Ti on the oxidation behaviour and mechanical properties of L<sub>12</sub>-strengthened FeCoCrNi high-entropy alloys. *Corros. Sci.* **2021**, *184*, 109365. [[CrossRef](#)]
25. Kong, D.; Guo, J.; Liu, R.W.; Zhang, X.H.; Song, Y.P.; Li, Z.X.; Guo, F.J.; Xing, X.F.; Xu, Y.; Wang, W. Effect of remelting and annealing on the wear resistance of AlCoCrFeNiTi<sub>0.5</sub> high entropy alloys. *Intermetallics* **2019**, *114*, 106560. [[CrossRef](#)]
26. Shi, Y.Z.; Yang, B.; Liaw, P. Corrosion-Resistant High-Entropy Alloys: A Review. *Metals* **2017**, *7*, 43. [[CrossRef](#)]
27. Chen, M.; Shi, X.H.; Yang, H.J.; Liaw, P.K.; Gao, M.C.; Hawk, J.A.; Qiao, J.W. Wear behavior of Al<sub>0.6</sub>CoCrFeNi high-entropy alloys: Effect of environments. *J. Mater. Res.* **2018**, *33*, 3310–3320. [[CrossRef](#)]
28. Li, Y.Z.; Shi, Y. Microhardness, wear resistance, and corrosion resistance of Al<sub>x</sub>CrFeCoNiCu high-entropy alloy coatings on aluminum by laser cladding. *Opt. Laser Technol.* **2021**, *134*, 106632. [[CrossRef](#)]
29. Chang, F.; Cai, B.J.; Zhang, C.; Huang, B.; Li, S.; Dai, P.Q. Thermal stability and oxidation resistance of FeCr<sub>x</sub>CoNiB high-entropy alloys coatings by laser cladding. *Surf. Coat. Technol.* **2019**, *359*, 132–140. [[CrossRef](#)]
30. Zhang, G.Z.; Liu, H.; Tian, X.H.; Chen, P.J.; Yang, H.F.; Hao, J.B. Microstructure and Properties of AlCoCrFeNiSi High-Entropy Alloy Coating on AISI 304 Stainless Steel by Laser Cladding. *J. Mater. Eng. Perform.* **2020**, *29*, 278–288. [[CrossRef](#)]
31. Senkov, O.N.; Wilks, G.B.; Miracle, D.B.; Chuang, C.P.; Liaw, P.K. Refractory high-entropy alloys. *Intermetallics* **2010**, *18*, 1758–1765. [[CrossRef](#)]
32. Juan, C.C.; Tsai, M.H.; Tsai, C.W.; Lin, C.M.; Wang, W.R.; Yang, C.C.; Chen, S.K.; Lin, S.J.; Yeh, J.W. Enhanced mechanical properties of HfMoTaTiZr and HfMoNbTaTiZr refractory high-entropy alloys. *Intermetallics* **2015**, *62*, 76–83. [[CrossRef](#)]
33. Senkov, O.N.; Wilks, G.B.; Scott, J.M.; Miracle, D.B. Mechanical properties of Nb<sub>25</sub>Mo<sub>25</sub>Ta<sub>25</sub>W<sub>25</sub> and V<sub>20</sub>Nb<sub>20</sub>Mo<sub>20</sub>Ta<sub>20</sub>W<sub>20</sub> refractory high entropy alloys. *Intermetallics* **2011**, *19*, 698–706. [[CrossRef](#)]
34. Chang, C.H.; Titus, M.S.; Yeh, J.W. Oxidation Behavior between 700 and 1300 °C of Refractory TiZrNbHfTa High-Entropy Alloys Containing Aluminum. *Adv. Eng. Mater.* **2018**, *20*, 1700948. [[CrossRef](#)]
35. Liu, C.M.; Wang, H.M.; Zhang, S.Q.; Tang, H.B.; Zhang, A.L. Microstructure and oxidation behavior of new refractory high entropy alloys. *J. Alloys Compd.* **2014**, *583*, 162–169. [[CrossRef](#)]

36. Gorr, B.; Azim, M.; Christ, H.J.; Mueller, T.; Schliephake, D.; Heilmaier, M. Phase equilibria, microstructure, and high temperature oxidation resistance of novel refractory high-entropy alloys. *J. Alloys Compd.* **2015**, *624*, 270–278. [[CrossRef](#)]
37. Cao, Y.K.; Liu, Y.; Liu, B.; Zhang, W.D.; Wang, J.W.; Meng, D.U. Effects of Al and Mo on high temperature oxidation behavior of refractory high entropy alloys. *Trans. Nonferrous Metal. Soc.* **2019**, *29*, 1476–1483. [[CrossRef](#)]
38. Jayaraj, J.; Thirathipviwat, P.; Han, J.; Gebert, A. Microstructure, mechanical and thermal oxidation behavior of AlNbTiZr high entropy alloy. *Intermetallics* **2018**, *100*, 9–19. [[CrossRef](#)]
39. Chen, L.; Wang, Y.Y.; Hao, X.H.; Zhang, X.W.; Liu, H.X. Light-weight refractory high entropy alloy coating by laser cladding on Ti-6Al-4V surface. *Vacuum* **2021**, *183*, 109823. [[CrossRef](#)]
40. Hamed, N.Z.; Ali-Reza, K.R.; Jalil, V.K. Design of a low density refractory high entropy alloy in non-equiatomic W-Mo-Cr-Ti-Al system. *Vacuum* **2020**, *181*, 109614. [[CrossRef](#)]
41. Han, Z.D.; Luan, H.W.; Liu, X.; Chen, N.; Li, X.Y.; Shao, Y.; Yao, K.F. Microstructures and mechanical properties of Ti<sub>x</sub>NbMoTaW refractory high-entropy alloys. *Mater. Sci. Eng. A.* **2018**, *712*, 380–385. [[CrossRef](#)]
42. Bhardwaj, V.; Zhou, Q.; Zhang, F.; Han, W.C.; Du, Y.; Hua, K.; Wang, H.F. Effect of Al addition on the microstructure, mechanical and wear properties of TiZrNbHf refractory high entropy alloys. *Tribol. Int.* **2021**, *160*, 107031. [[CrossRef](#)]
43. Senkov, O.N.; Senkova, S.V.; Woodward, C. Effect of aluminum on the microstructure and properties of two refractory high-entropy alloys. *Acta. Mater.* **2014**, *68*, 214–228. [[CrossRef](#)]
44. Yang, X.; Zhang, Y.; Liaw, P.K. Microstructure and Compressive Properties of NbTiV<sub>2</sub>TaAl<sub>x</sub> High Entropy Alloys. *Procedia Eng.* **2012**, *36*, 292–298. [[CrossRef](#)]
45. Stepanov, N.D.; Shaysultanov, D.G.; Salishchev, G.A.; Tikhonovsky, M.A. Structure and mechanical properties of a light-weight AlNbTiV high entropy alloy. *Mater. Lett.* **2015**, *142*, 153–155. [[CrossRef](#)]
46. Zheng, Z.P.; Jin, X.; Bai, Y.C.; Yang, Y.; Ni, C.B.; Lu, W.F.; Wang, H. Microstructure and anisotropic mechanical properties of selective laser melted Ti6Al4V alloy under different scanning strategies. *Mater. Sci. Eng. A.* **2022**, *831*, 142236. [[CrossRef](#)]
47. Kurz, W.; Bezencon, C.; Gäumann, M. Columnar to equiaxed transition in solidification processing. *Sci. Technol. Adv. Mater.* **2001**, *2*, 185. [[CrossRef](#)]
48. Zhang, Y.L.; Li, J.; Zhang, Y.Y.; Kang, D.N. Evolution in microstructure and high-temperature oxidation behaviors of the laser-cladding coatings with the Si addition contents. *J. Alloys Compd.* **2020**, *827*, 154131. [[CrossRef](#)]
49. Guo, S.; Hu, Q.; Ng, C.; Liu, C.T. More than entropy in high-entropy alloys: Forming solid solutions or amorphous phase. *Intermetallics* **2013**, *41*, 96–103. [[CrossRef](#)]
50. Cai, Z.B.; Pang, X.J.; Cui, X.F.; Wen, X.; Liu, Z.; Dong, M.L.; Li, Y.; Jin, G. In Situ Laser Synthesis of High Entropy Alloy Coating on Ti-6Al-4V Alloy: Characterization of Microstructure and Properties. *Mater. Sci. Forum.* **2017**, *898*, 643–650. [[CrossRef](#)]
51. Ye, X.Y.; Ma, M.X.; Cao, Y.X.L.; Liu, W.J.; Ye, X.H.; Gu, Y. The Property Research on High-entropy Alloy Al<sub>x</sub>FeCoNiCuCr Coating by Laser Cladding. *Phys. Procedia* **2011**, *12*, 303–312. [[CrossRef](#)]
52. Jiang, P.F.; Zhang, C.H.; Zhang, S.; Zhang, J.B.; Chen, J.; Liu, Y. Fabrication and wear behavior of TiC reinforced FeCoCrAlCu-based high entropy alloy coatings by laser surface alloying. *Mat. Chem. Phys.* **2020**, *255*, 123571. [[CrossRef](#)]
53. Cheng, J.B.; Liu, D.; Liang, X.B.; Chen, Y.X. Evolution of microstructure and mechanical properties of in situ synthesized TiC-TiB<sub>2</sub>/CoCrCuFeNi high entropy alloy coatings. *Surf. Coat. Technol.* **2015**, *281*, 109–116. [[CrossRef](#)]
54. Li, X.F.; Feng, Y.H.; Liu, B.; Yi, D.H.; Yang, X.H.; Zhang, W.D.; Chen, G.; Liu, Y.; Bai, P.K. Influence of NbC particles on microstructure and mechanical properties of AlCoCrFeNi high-entropy alloy coatings prepared by laser cladding. *J. Alloys Compd.* **2019**, *788*, 485–494. [[CrossRef](#)]
55. Guo, Y.J.; Li, C.J.; Zeng, M.; Wang, J.Q.; Deng, P.; Wang, Y. In-situ TiC reinforced CoCrCuFeNiSi<sub>0.2</sub> high-entropy alloy coatings designed for enhanced wear performance by laser cladding. *Mat. Chem. Phys.* **2020**, *242*, 122522. [[CrossRef](#)]
56. Guo, Y.X.; Shang, X.J.; Liu, Q.B. Microstructure and properties of in-situ TiN reinforced laser cladding CoCr<sub>2</sub>FeNiTi high-entropy alloy composite coatings. *Surf. Coat. Technol.* **2018**, *344*, 353–358. [[CrossRef](#)]
57. Park, B.J.; Chang, H.J.; Kim, D.H.; Kim, W.T. In situ formation of two amorphous phases by liquid phase separation in Y-Ti-Al-Co alloy. *Appl. Phys. Lett.* **2004**, *85*, 6353–6355. [[CrossRef](#)]
58. Guo, S.; Ng, C.; Lu, J.; Liu, C.T. Effect of valence electron concentration on stability of fcc or bcc phase in high entropy alloys, *J. Appl. Phys.* **2011**, *109*, 103505. [[CrossRef](#)]
59. Gao, M.C.; Yeh, J.W.; Liaw, P.K.; Zhang, Y. *High-Entropy Alloys: Fundamentals and Applications*; Springer International Publishing: Cham, Switzerland, 2016. [[CrossRef](#)]
60. Zhao, P.; Li, J.; Zhang, Y.; Li, X.; Xia, M.M.; Yuan, B.G. Wear and high-temperature oxidation resistances of AlNbTaZr<sub>x</sub> high-entropy alloys coatings fabricated on Ti6Al4V by laser cladding. *J. Alloys Compd.* **2021**, *862*, 158405. [[CrossRef](#)]
61. Jamilpanah, L.; Khademi, I.; Gharehbagh, J.S.; Mohseni, S.A.; Mohseni, S.M. Promising memristive behavior in MoS<sub>2</sub>-MoO<sub>2</sub>-MoO<sub>3</sub> scalable composite thin films. *J. Alloys Compd.* **2020**, *835*, 155291. [[CrossRef](#)]
62. Xu, C.; Gao, W. Pilling-Bedworth ratio for oxidation of alloys. *Mat. Res. Innovat.* **2000**, *3*, 231–235. [[CrossRef](#)]